Neuroinvasion and anosmia are independent phenomena upon infection with SARS-CoV-2 and its variants

Short title: Brain invasion by SARS-CoV-2

Guilherme Dias de Melo[1], Victoire Perraud[1§], Flavio Alvarez[2,3§], Alba Vieites-Prado[4§], Seonhee Kim[1], Lauriane Kergoat[1], Bettina Salome Trüeb[5], Magali Tichit[6], Aurèle Piazza[7], Agnès Thierry[7], David Hardy[6], Nicolas Wolff[2], Sandie Munier[8], Romain Koszul[7], Etienne Simon-Lorière[9], Volker Thiel[10], Marc Lecuit[11], Pierre-Marie Lledo[12], Nicolas Renier[4], Florence Larrous[1#], Hervé Bourhy[1#*]

[1] Institut Pasteur, Université Paris Cité, Lyssavirus Epidemiology and Neuropathology Unit, F-75015 Paris, France

[2] Institut Pasteur, Université Paris Cité, Channel Receptors Unit, F-75015 Paris, France

[3] Sorbonne Université, Collège Doctoral, F-75005 Paris, France

[4] Institut du Cerveau et de la Moelle Épinière, Laboratoire de Plasticité Structurale, Sorbonne Université, INSERM U1127, CNRS UMR7225, 75013 Paris, France

[5] Institute of Virology and Immunology (IVI), Bern, Switzerland ; Department of Infectious Diseases and Pathobiology, Vetsuisse Faculty, University of Bern, Bern, Switzerland

[6] Institut Pasteur, Université Paris Cité, Histopathology Platform, F-75015 Paris, France

[7] Institut Pasteur, Université Paris Cité, Spatial Regulation of Genomes Laboratory, F-75015 Paris, France

[8] Institut Pasteur, Université Paris Cité, Molecular Genetics of RNA viruses Unit, F-75015 Paris, France

[9] Institut Pasteur, Université Paris Cité, Evolutionary Genomics of RNA Viruses Group, F-75015 Paris, France

[10] Multidisciplinary Center for Infectious Diseases, University of Bern, Bern, Switzerland

[11] Institut Pasteur, Université Paris Cité, Biology of Infection Unit, F-75015 Paris, France ; INSERM U1117, 75015 Paris, France ; Université Paris Cité, Necker-Enfants Malades University Hospital, Division of Infectious Diseases and Tropical Medicine, Institut Imagine, AP-HP, 75015 Paris, France

[12] Institut Pasteur, Université Paris Cité, Perception and Memory Unit, F-75015 Paris, France ; CNRS UMR3571, 75015 Paris, France

[§] these authors contributed equally
[#] senior author
[*] corresponding author: herve.bourhy@pasteur.fr

SUMMARY

Anosmia was identified as a hallmark of COVID-19 early in the pandemic, however, with the emergence of variants of concern, the clinical profile induced by SARS-CoV-2 infection has changed, with anosmia being less frequent. Several studies have focused on the neuropathogenesis of the original SARS-CoV-2, but little is known about the neuropathological potential of the variants. Here, we assessed the clinical, olfactory and inflammatory conditions of golden hamsters infected with the original SARS-CoV-2, its ORF7-deleted mutant, and three variants: Gamma, Delta and Omicron/BA.1. We show that infected animals developed a variant-dependent clinical disease, and that the ORF7 of SARS-CoV-2 contribute to causing olfactory disturbances. Conversely, all SARS-CoV-2 variants were found to be neuroinvasive, regardless of the clinical presentation they induce. With newly-generated nanoluciferase-expressing SARS-CoV-2, we validated the olfactory pathway as a main entry point towards the brain, confirming that neuroinvasion and anosmia are independent phenomena upon SARS-CoV-2 infection.

Keywords: host-pathogen interaction, host adaptation, COVID-19, neurotropism, olfaction, olfactory bulbs, central nervous system, reverse genetics

Graphical asbtract

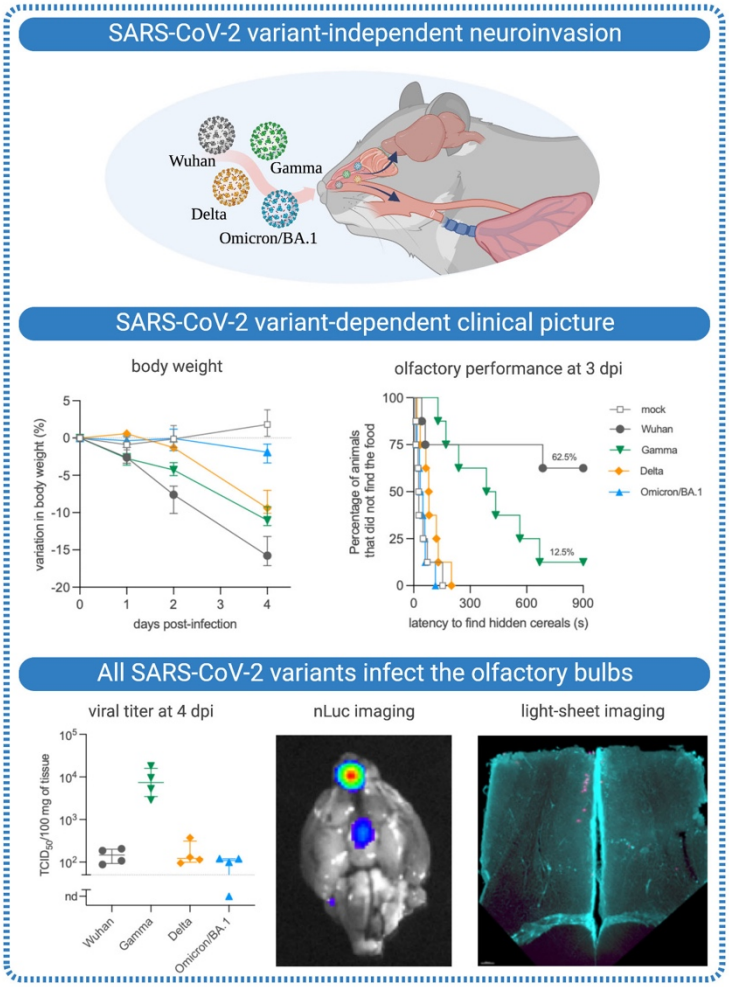

INTRODUCTION

The COVID-19 pandemic remains a major contemporary worldwide public health problem. Since the beginning of the pandemic in December 2019, more than 500 million cases have been confirmed, all SARS-CoV-2 variants combined (WHO, 2022). The original SARS-CoV-2 (Wuhan) gave rise to different variants of concern (VoCs) in the first year of the pandemic (B.1.1.7, B.1.351, P.1), which were almost totally replaced by the VoC Delta (B1.617.2) in 2020, by the VoC Omicron/BA.1 (B.1.1.529) in 2021 and other Omicron lineages (BA.2, BA.4, BA.5) in 2022 (WHO, 2022).

SARS-CoV-2 infects cells of the upper and lower airways, and COVID-19 manifests by a multitude of respiratory and extra-respiratory symptoms, including neurological manifestations, ranging from headache and dizziness to anosmia, ageusia and even stroke (Chou et al., 2021; Klimek et al., 2022; Paterson et al., 2020). The neuropathology of COVID-19 is currently considered to be a consequence of inflammation and hypoxia, rather than direct viral invasion into the CNS (Ruz-Caracuel et al., 2022; Thakur et al., 2021). However, with the emergence of the VoCs, and the increasing rate of vaccination or previous infection, the symptomatology of COVID-19 has changed. In this context, the clinical picture induced by the VoC Omicron/BA.1 is less severe or sometimes asymptomatic, with a higher rate of upper airways involvement, sparing the olfactory mucosa and consequently a lower incidence of anosmia, initially considered a hallmark of COVID-19 (Boscolo-Rizzo et al., 2022; Cardoso et al., 2022; Chen et al., 2022; Christensen et al., 2022; Garrett et al., 2022; Vihta et al., 2022).

Previously, we determined that the infection of olfactory sensory neurons and loss of cilia in the olfactory mucosa caused by SARS-CoV-2 Wuhan in humans and Syrian hamsters and local inflammation were associated to olfaction loss, as well as neuroinflammation in the olfactory bulbs and that hamsters were relevant models for the study of the pathogenesis of SARS-CoV-2 infection (Chan et al., 2020; de Melo et al., 2021; Sia et al., 2020). Other authors reported persistent microgliosis in the olfactory bulbs of infected hamsters (Käufer et al., 2022), and differences in the neuroinvasiveness and neurovirulence of VoCs have been described (Bauer et al., 2022b). Additionally, other authors have attempted to compare VoCs pathogenicity in hamsters (Halfmann et al., 2022; McMahan et al., 2022; Mohandas et al., 2022), but studies relating SARS-CoV-2 brain invasion to neurological symptoms are lacking.

Here, we identified that SARS-CoV-2 Wuhan and the VoCs Gamma, Delta and Omicron/BA.1 are all capable of invading the brain of Syrian hamsters and of eliciting a tissue-specific inflammatory response. Using reverse genetics-generated bioluminescent viruses, we demonstrate that SARS-CoV-2 infects the olfactory bulbs, but the clinical profile, including the olfactory performance, is highly dependent on the variant. Further, deletion of the ORF7ab sequence in the ancestral virus reduces

the incidence of olfaction loss without affecting the clinical picture nor the neuroinvasiviness. Accordingly, this work validates the olfactory pathway as the main entry route by SARS-CoV-2 into the brain and corroborates the neurotropic potential of SARS-CoV-2 variants. Neuroinvasion and anosmia are therefore independent phenomena upon SARS-CoV-2 infection.

RESULTS

SARS-CoV-2 induces a clinical disease in hamsters, with a VoC-related severity difference

We first investigated the differences in the clinical picture induced by different SARS-CoV-2 VoCs in comparison with the ancestral virus (Wuhan). We first tested the *in vitro* growth curves of these viruses in Vero-E6 cells, and found no significant differences (Fig. S1A). Then, male golden hamsters were inoculated intranasally with $6x10^4$ PFU of SARS-CoV-2 Wuhan or the VoCs Gamma, Delta or Omicron/BA.1 and followed them up during 4 days post-infection (dpi). All SARS-CoV-2-infected animals presented a progressive loss of weight; however, a variant effect was observed (Kruskal-Wallis P<0.0001, Fig. 1A-B), with SARS-CoV-2 Wuhan-infected animals presenting the most intense median weight loss (15.8%, interquartile range 'IQR' 3.9%), followed by Gamma-infected animals (11.0%, IQR 2.6%), Delta-infected animals (9.4%, IQR 3.1%) and Omicron/BA.1-infected animals (1.9%, IQR 2.5%). Non-specific sickness-related clinical signs (ruffled fur, slow movement, apathy) followed the same pattern (Kruskal-Wallis P<0.0001, Fig. 1D-E), with SARS-CoV-2 Wuhan-infected animals presenting the worse clinical picture, followed by Gamma- and Delta-infected animals, while Omicron/BA.1-infected animals presented a delayed manifestation of mild signs, clinically observable at 4 dpi only.

Olfaction loss is a typical clinical sign of SARS-CoV-2 Wuhan-infected hamsters (de Melo *et al.*, 2021), however olfactory deficit differed according to the different VoCs (Chi-square for trend P<0.0001): 62.5% (5/8) of SARS-CoV-2 Wuhan-infected animals presented loss of olfaction (Log-rank test compared to the mock P=0.0012), only 12.5% (1/8) of Gamma-infected animals lost olfaction completely with 62.5% (5/8) presenting an impaired olfactory performance (*i.e.* longer time to find the hidden cereals) (Log-rank test compared to the mock P<0.0001). In contrast, none of the Delta- and Omicron/BA.1-infected animals presented signs of olfactory impairment (Fig. 1G-H).

Regarding lung pathology, as for the other clinical parameters, lung enlargement and lung weight-to-body weight (LW/BW) ratio were significantly higher in SARS-COV-2 Wuhan-infected animals; Gamma- and Delta-infected animals presented intermediate values, whereas Omicron/BA.1-infected animals' values were close to those of the ones of mock-infected animals (Kruskal-Wallis P<0.0001, Fig. 1C and 1F). Likewise, the histopathological findings in the lungs followed the same tendency: congestion, edema, mononuclear cells infiltration, thickening of the

alveolar walls and bronchiolar epithelium desquamation were observed in all infected animals (Fig. S2A), along with a diffuse SARS-CoV-2 nucleoprotein staining (Fig. S2B), with more severe alterations observed in the lungs of SARS-COV-2 Wuhan-infected animals than in Gamma-, Delta-, and Omicron/BA.1-infected hamsters.

In a multivariate analysis of clinical parameters recorded at 4 dpi, the two-first principal components explained 92.4% of sample variability. Body weight loaded negatively to PC1 (principal component) and negatively correlated with the clinical score and the LW/BW ratio, whereas the olfactory performance loaded positively to PC2 (Fig. S3A). In the principal component analysis (PCA) plot regarding tissue-related inflammation, the difference among groups was marked: mock and Omicron/BA.1-infected animals loaded homogeneously and relatively close, followed by the Delta-infected animals. SARS-COV-2 Wuhan- and Gamma-infected animals loaded in a more dispersed way, far away from the other VoCs, effect of the olfactory performance results (Fig. S3C).

SARS-CoV-2-infected airways respond to the infection regardless of the viral variants

Next, we measured the viral titer and RNA loads in the upper airways (nasal turbinates), and in the lower airways (lung). Infectious viruses were detected in the nasal turbinates and in the lungs of all infected hamsters regardless of the VoC, however, a variant effect was observed, with the highest values for the Gamma-infected animals, and the lowest values for the Omicron/BA.1-infected animals (Kruskal-Wallis $P<0.0001$, Fig. 2A). Genomic and sub-genomic SARS-CoV-2 RNA were detected equally in the lungs of all infected animals; but differently in the nasal turbinates, regardless of the positivity of all samples, Delta-infected animals presented the highest viral load (Kruskal-Wallis $P=0.0023$, Fig. 2B).

Both the upper and lower airways responded to the infection by all VoCs (Fig. 2CD), but with a tissue-specific inflammatory signature: in the lungs, *Mx2, Il-6, Cxcl10* and *Il-10* were upregulated for all VoCs, and the highest in SARS-COV-2 Wuhan-infected animals (Fig. 2C). In the nasal turbinates, the gene expression of *Ifn-β* and *Il-6* presented the highest values in SARS-COV-2 Wuhan-infected animals and the lowest in Omicron/BA.1-infected animals. *Mx2*, *Cxcl10* and *Il-10* expression were the highest in Delta-infected animals while Omicron/BA.1-infected animals showed the lowest levels (Fig. 2D). To better appreciate the tissue- *vs.* VoC-related gene expression, we performed a multivariate analysis of these data. Interestingly, the two-first principal components explained 79.6% of sample variability (Fig. S3B). In the PCA plots, the nasal turbinates of all infected hamsters were loaded together (Fig. S3D), whereas in the lungs, only SARS-COV-2 WUHAN- and Delta-infected animals loaded in the same area, effect of *Il-6, Cxcl10* and *Il-10* (Fig. S3D).

SARS-CoV-2 neuroinvasion and neuroinflammation in the olfactory bulbs

After establishing the clinical and inflammatory profile of the infected animals, we aimed to assess the effect of infection on the olfactory bulbs. Remarkably, even if the olfactory performance differed according to the VoCs (Fig. 1G-H), positive viral titers were detected in the olfactory bulbs of animals from all infected groups, with Gamma-infected animals presenting the highest titer at 4 dpi (Kruskal-Wallis P=0.0096, Fig. 2A). These findings were corroborated by the detection of genomic viral RNA in the olfactory bulbs of animals from all infected groups as well, but viral RNA load was higher in SARS-COV-2 WUHAN-infected animals (Kruskal-Wallis P=0.0104, Fig. 2B). Conversely, sub-genomic RNA was below the detection limit in these samples, indicating the absence of productive SARS-CoV-2 replication.

The olfactory bulbs presented an intrintriguing inflammatory profile. The antiviral *Mx2* gene, along with the inflammatory genes *Ifn-β*, *Il-6* and *Cxcl10* were highly upregulated in the olfactory bulbs of hamsters infected by all VoCs, including Delta and Omicron/BA.1 (Fig. 2E), regardless of the normal olfactory performance in the food-finding test (Fig. 1 G-H), yet *Il-10* expression was upregulated only in the olfactory bulbs of SARS-COV-2 Wuhan- and Delta-infected animals (compared to the mock). Unexpectedly, the gene expression of these selected targets tended to be higher in the olfactory bulbs of Delta-infected animals, including *Tnf-α*, which expression was not significative for SARS-COV-2 Wuhan-, Gamma- and Omicron/BA.1-infected animals (Fig. 2E). In a multivariate analysis for tissue- and VoC-related gene expression, the olfactory bulbs from SARS-COV-2 Wuhan-infected animals tended to load in proximity to the corresponding nasal turbinates (effect of *Il-6*, *Cxcl10* and *Il-10*), whereas olfactory bulbs from Gamma-, Delta- and Omicron/BA.1-infected animals loaded separately, possibly reflecting the impact of *Mx2*, *Tnf-α* and *Ifn-β* differential expression (Fig. S3D).

Having detected the virus in the olfactory bulbs using virologic and molecular techniques, we aimed to visualize the infection. We examined the SARS-CoV-2/W distribution in the whole brain by combining whole-head tissue clearing with light sheet microscopy imaging using iDISCO+ (Renier et al., 2014). At 4 dpi, all SARS-COV-2 Wuhan-infected hamsters displayed a diffuse viral distribution in the nasal cavity: nasal turbinates and olfactory epithelium (Fig. 3A and Video S1). Along the same lines, all SARS-COV-2 Wuhan-infected animals presented SARS-CoV-2 in the olfactory bulbs in sparse neurons, localized in the proximity of the olfactory nerve entry point (Fig. 3B and Video S2). No virus was observed in other areas of the brain and no alteration in the vascular network was observed.

We next used a complementary method to visualize the infection of the olfactory bulbs. To this end, we generated recombinant viruses that express the nanoluciferase by reverse genetics (SARS-CoV-2 Wuhan_nLuc and Delta_nLuc; Fig. S1B and S4A). The disease profile induced by these two recombinant viruses was similar to the profile induced by the wild-type parental viruses (Fig. 3C). *In vivo* imaging of infected hamsters was performed at 4 dpi using fluorofurimazine (FFz) as substrate. Very low positive signals were observed in the nasal cavity region, possibly due to the thickness of

the skin and bones that could block the light emission, but significantly higher in the Wuhan_nLuc than the Delta_nLuc (Mann Whitney P=0.0286, Fig. S4BC). More sensitive results were obtained during the *ex vivo* imaging. After euthanasia, the lungs and brains were collected and imaged. Positive signals in the lungs were obtained at the same intensity for both viruses (Fig. 3D), and presented a multi-focal/diffuse distribution (Fig. 3E and S4D). The brains were imaged in the ventral position in order to better expose the olfactory bulbs. Intense luminescent signals were recorded from the brains of hamsters infected with either viruses; when placing the ROI (region of interest) exclusively in the olfactory bulbs, intensity was higher in Wuhan_nLuc (Mann Whitney P=0.0286); conversely, when considering the whole brain ventral area, intensity was higher in Delta_nLuc (Mann Whitney P=0.0286). The ratio of olfactory bulbs/brain signals was 4-fold higher for Wuhan_nLuc than Delta_nLuc (Mann Whitney P=0.0286, Fig. 3C and S4D), which might reflect the higher replication rate detected in the olfactory bulbs infected by the SARS-CoV-2/W (Fig. 2B). Despite intensity differences, the olfactory bulbs are the major infected structure in the brain, and sagittal views of the brain indicate that the origin of the luminescent signal is the ventral part of the olfactory bulbs, which is situated above the olfactory epithelium in the nasal cavity (Fig. 3E and S4E).

Anosmia is not associated with viral load or infection of the olfactory bulbs

All tested SARS-CoV-2 variants were found to be able to invade the CNS and infect the olfactory bulbs, but the incidence of olfactory dysfunctions varied according to the VoC, with hamsters infected with Delta and Omicron/BA.1 presenting no signs of anosmia (Fig. 1G-H). Several mutations on the spike distinguish the different VoCs. Furthermore, some VoC isolates also present deletions in the ORF7 sequence (Jelley et al., 2022; Mazur-Panasiuk et al., 2021; Panzera et al., 2021; Pyke et al., 2021), including the Delta isolate used in the present study (deletion spanning positions 27507 to 27541 of the reference SARS-CoV-2 Wuhan genome). Since a possible link between ORF7b and olfaction loss has been proposed (Fogeron et al., 2021), we constructed a recombinant SARS-CoV-2 based on the CoV-2/W backbone, where the ORF7ab sequence was replaced by that of GFP (SARS-CoV-2 Wuhan/ΔORF7ab) (Fig. S1C). Remarkably, the clinical profile exhibited by Wuhan/Δ ORF7ab-infected hamsters was similar to the one caused by the wild-type SARS-CoV-2 Wuhan (Fig. 4A-D), showing that ORF7ab is not essential for viral infection and replication. However, the olfaction loss incidence decreased significantly; only 25% (2/8) of the infected animals presented signs of anosmia, in contrast to the 62.5% (5/8) observed in CoV-2/SARS-COV-2 Wuhan-infected hamsters (Chi-square for trend P=0.0060; Fig. 4E). Despite this reduction in anosmia incidence, Wuhan/Δ ORF7ab was still detected in the airways and in the olfactory bulbs of infected animals, with even higher titers (Fig. 4F-G).

Further, in order to test if the viral inoculum could influence the neuroinvasiveness of SARS-CoV-2 and the incidence of olfactory dysfunctions, we infected hamsters with a 2-log lower infectious dose of CoV-2/W ($6x10^2$ PFU). These animals were submitted to the same clinico-behavioral tests described above. In the acute phase of the infection, up to 4 dpi, the low infectious dose induced similar body weight loss and clinical score as the animals infected with the initial inoculum, as well as infectious viral titers in the airways and in the olfactory bulbs (Fig. 4). Surprisingly, despite the presence of infectious virus in the olfactory bulbs, animals infected with a lower infectious dose presented a lower incidence of olfactory dysfunction (25%, 2/8).

DISCUSSION AND CONCLUSIONS

The neurotropism of SARS-CoV-2 is still a matter of debate (Bauer et al., 2022a). While studies on natural infection in humans and experimental infection in animal models reported brain infection by SARS-CoV-2 (de Melo *et al.*, 2021; Matschke et al., 2020; Meinhardt et al., 2021; Rutkai et al., 2022; Song et al., 2021), including in *in vitro* human models of infection (Pellegrini et al., 2020; Ramani et al., 2020), others failed to detect SARS-CoV-2 in the nervous tissue (Khan et al., 2021; Thakur *et al.*, 2021). Despite this open question, the impact of SARS-CoV-2 infection on the brain is undeniable (Douaud et al., 2022; Helms et al., 2020; Paterson *et al.*, 2020; Yang et al., 2021). Most of these published data is related to the original SARS-CoV-2 (Wuhan), however, less information concerning VoCs neuropathogenesis is available (Chen *et al.*, 2022). Here we show that all evaluated SARS-CoV-2 viruses (Wuhan, Gamma, Delta and Omicron/BA.1) are able to invade the brain, most likely via the olfactory bulbs, and of promoting inflammation.

Despite this shared neuroinvasiveness, disease profile and airways responses are quite dependent on the SARS-CoV-2 variant. Indeed, we show that all VoCs can infect golden hamsters and promote lung inflammation, including Omicron/BA.1 differently from other reports (Abdelnabi et al., 2022; Halfmann *et al.*, 2022), probably due to infectious doses or viral isolates. A “variant-effect” in the clinical presentation and in the tissue-related inflammation was evident, with disease severity presenting the following order: SARS-CoV-2 Wuhan > Gamma > Delta > OmicronBA.1, which supports the hypothesis that Omicron/BA.1 evolution has resulted in a tropism more restricted to the upper respiratory tract, thereby causing a less severe clinical disease (Armando et al., 2022; Chen *et al.*, 2022; Hui et al., 2022; Yuan et al., 2022). Notwithstanding, the neuroinvasiveness, neurotropism, and neurovirulence characteristics of Omicron/BA.1 is similar to the other SARS-CoV-2 variants. Indeed, the data presented herein give support to the neuroinvasive ability of SARS-CoV-2, as besides detection of viral RNA and isolation of infectious virus from the olfactory bulbs, we could clearly observe SARS-CoV-2 infected neurons in the brain of hamsters by light sheet microscopy.

Nevertheless in hamsters, unlike what has been reported in K18-hACE2 mice which ACE2 expression pattern is non-physiological and ectopic (Song *et al.*, 2021), SARS-CoV-2 Wuhan infection was restricted to the olfactory bulbs, without evidence of brain vasculature remodeling nor virus associated with blood vessels.

Olfactory bulb infection is therefore a common feature in the SARS-CoV-2 infectious process, regardless of the variant considered. An inflammation response was also observed in this tissue, with a common upregulation of the antiviral gene *Mx2*, regardless of the VoC. The reason why some VoCs do not cause olfaction loss is still an open question. The infection and inflammation of the olfactory bulbs, if involved in SARS-CoV-2-associated anosmia, does not seem to be enough to cause olfaction loss in the golden hamster. Aggressions to the olfactory mucosa, rather than the olfactory bulb, are indeed likely the main factors contributing to anosmia, as recovery from anosmia has been related to regeneration of the olfactory epithelium in hamsters (Reyna et al., 2022; Urata et al., 2021). Moreover, significant changes in the olfactory epithelium, such as apoptosis, architectural damages, inflammation, downregulation of odorant receptors and functional changes in olfactory sensory neurons, might also contribute, on top of the infection *per se*, to the occurrence of anosmia (Bourgon et al., 2022; Chen *et al.*, 2022; de Melo *et al.*, 2021; Kishimoto-Urata et al., 2022; Messlinger et al., 2022; Zazhytska et al., 2022). Therefore, it seems that infection and inflammation combined are needed to trigger anosmia, and the lower incidende of anosmia observed after infection by some VoCs is therefore linked to lower levels of inflammation.

Furthermore, besides mutations in the spike sequence in the SARS-CoV-2 variants genome, additional mutations may be present in other regions of the viral genome, including deletions in the ORF7a and ORF7b sequences (Jelley *et al.*, 2022; Mazur-Panasiuk *et al.*, 2021; Panzera *et al.*, 2021; Pyke *et al.*, 2021). ORF7a and ORF7b have been related to viral-induced apoptosis, and to interference with the innate immunity and the antiviral response (Aliyari et al., 2022; Hayn et al., 2021; Schaecher et al., 2007; Su et al., 2021), without, however, being essential to viral infection and replication (Schaecher et al., 2008; Silvas et al., 2021). Further, ORF7b has the potential to interfere with cell adhesion proteins in the olfactory mucosa (Fogeron *et al.*, 2021), and interestingly, a binary interaction between ORF7b and the human olfactory receptor OR1D5 has also been reported (Kim et al., 2021). Deletions or mutations in these regions may therefore play an additional role in the induction of olfactory disturbances, by preserving the architecture and structures of the olfactory epithelium. Another important point is that we can observe a similar clinical profile and low incidence of olfactory disturbances as SARS-CoV-2 Wuhan/ΔORF7ab by simply reducing the viral inoculum of SARS-CoV-2 Wuhan. Regardless of a comparative evolution of body weight loss and clinical score (Imai et al., 2020), anosmia was less frequent in animals infected with a low dose of SARS-CoV-2 Wuhan. This might be related to the less severe initial aggression suffered by the olfactory epithelium

due to lower infectious doses (Bryche et al., 2020; Urata *et al.*, 2021) and may also explain why other studies did not detect olfaction dysfunction despite detecting inflammatory changes in the brain (Frere et al., 2022).

Despite the occurrence or not of anosmia, SARS-CoV-2 can infect olfactory sensory neurons and the olfactory bulb (Chen *et al.*, 2022; de Melo *et al.*, 2021). SARS-CoV-2 neuroinvasion was hypothesized to occur by retrograde axonal flow via cranial nerves (olfactory, vagus, trigeminal) or by the hematogeneous route (Bauer *et al.*, 2022a; Bulfamante et al., 2021; DosSantos et al., 2020). The data presented herein do not support hematogenous diffusion of SARS-CoV-2 towards the brain, and supports hypothesis of the olfactory retrograde pathway as a preferential portal of entry (Ueha et al., 2022). Brain infection via the olfactory pathway therefore seems a common feature of coronaviruses (Dubé et al., 2018; Shi et al., 2022), regardless of clinical disease presentations. Finally, this study highlights that neuroinvasion and anosmia are therefore independent phenomena upon SARS-CoV-2 infection.

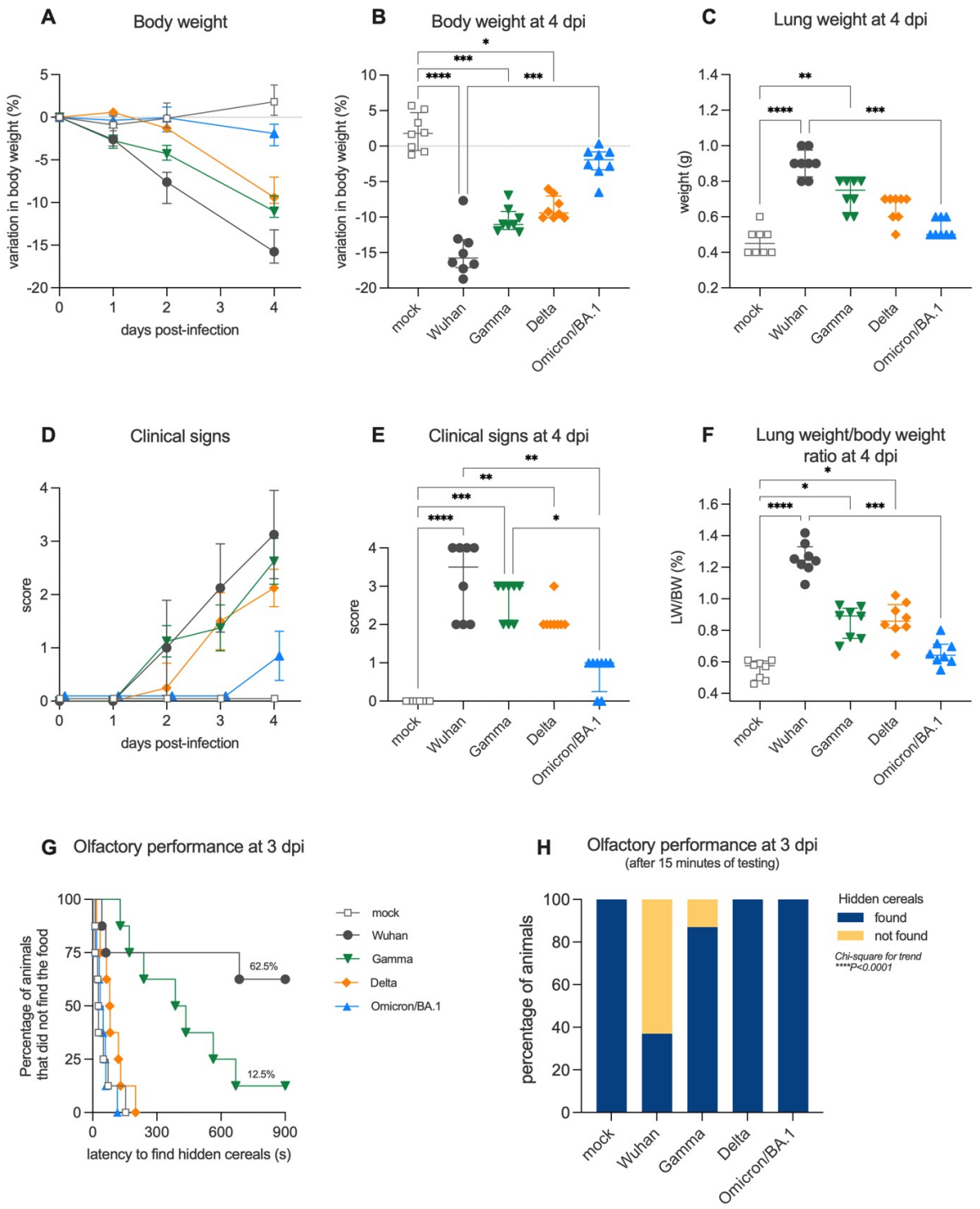

Figure 1. Clinical profile of hamsters infected with SARS-CoV-2 original virus (Wuhan) or the variants of concern (VoC) Gamma, Delta and Omicron/BA.1. AB. Body weight variation over four days post-infection. **C**. Lung weight measured at 4 dpi. **DE**. Clinical score over four days post-infection. The clinical score is based on a cumulative 0–4 scale: ruffled fur; slow movements; apathy; and absence of exploration activity. **F**. Lung weight-to-body weight ratio measured at 4 dpi. Horizontal lines indicate median and the interquartile range (n=8/group). Kruskall-Wallis test followed by the Dunn's multiple comparisons test (*P<0.05, **P<0.01, ***P<0.001, ****P<0.0001). **GH**. Olfactory performance measured at 3 days post-infection (dpi). The olfaction test is based on the hidden (buried) food finding test. Curves represent the olfactory performance of animals during the test (G) and bars represent the final results (H) (n=8/group). Chi-square test for trend (****P<0.0001). See Supplementary Figures 1 and 2.

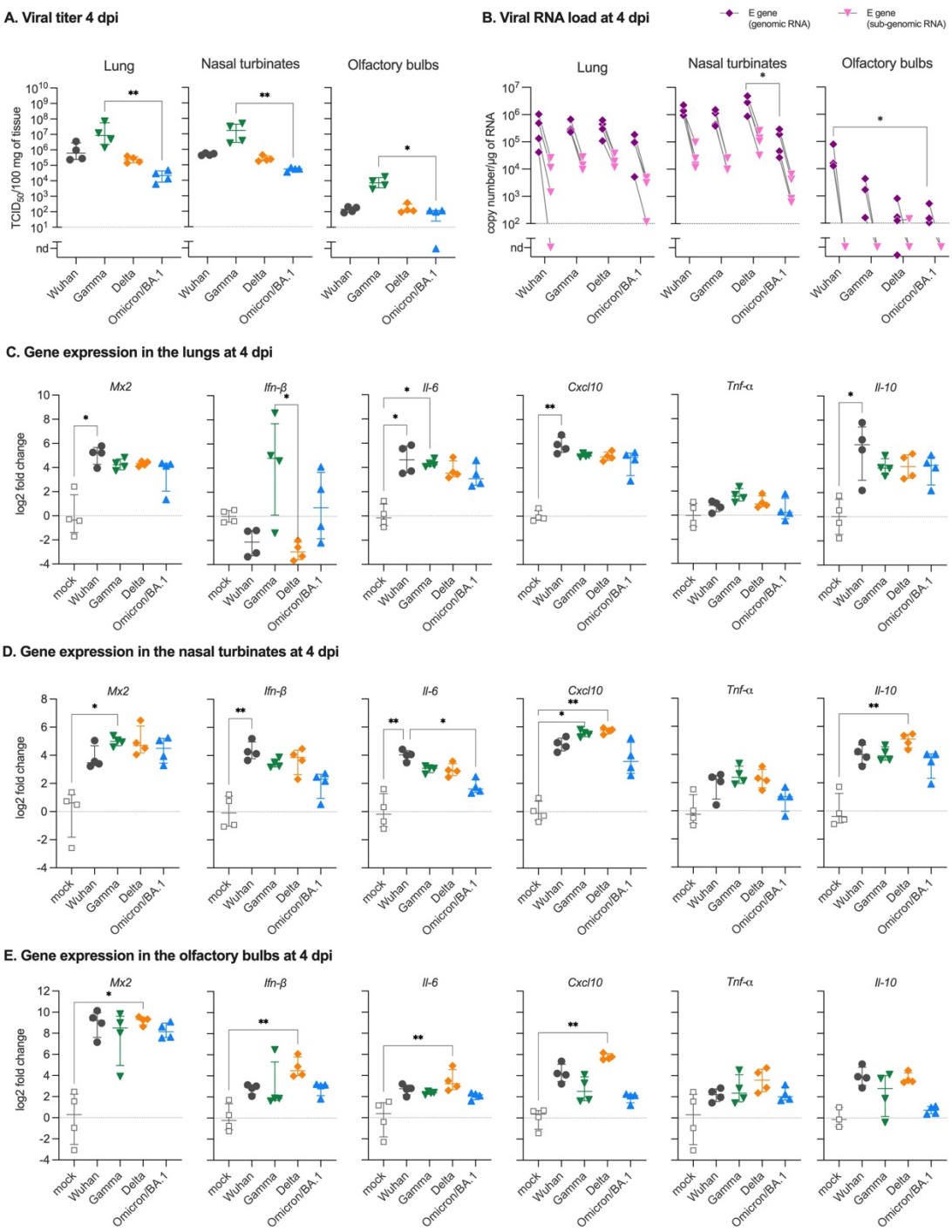

Figure 2. Virologic assessment and gene expression of selected immune mediators in different tissues of hamsters infected with SARS-CoV-2 original virus (Wuhan) or the variants of concern (VoC) Gamma, Delta and Omicron/BA.1. A. Infectious viral titers in the lung, nasal turbinates and olfactory bulbs at 4 days post-infection (dpi) expressed as $TCID_{50}$ per 100 mg of tissue. Horizontal lines indicate median and the interquartile range (n=4/group). **B.** SARS-CoV-2 viral RNA load detected in the lung, nasal turbinates and olfactory bulbs at 4 dpi. Genomic and sub-genomic viral RNA were assessed based on the E gene sequence. Horizontal lines indicate median and the interquartile range Gray lines connect symbols from the same animals (n=4/group). **C-E.** Gene expression values in the lung (C), nasal turbinates (D) and olfactory bulbs (E) of *Mx2, Ifn-*β*, Il-6, Cxcl10, Tnf-*α and *Il-10* at 4 dpi. Horizontal lines indicate median and the interquartile range (n=4/group). Kruskall-Wallis test followed by the Dunn's multiple comparisons test (*P<0.05, **P<0.01). nd: not detected. See Supplementary Figures 1 and 2.

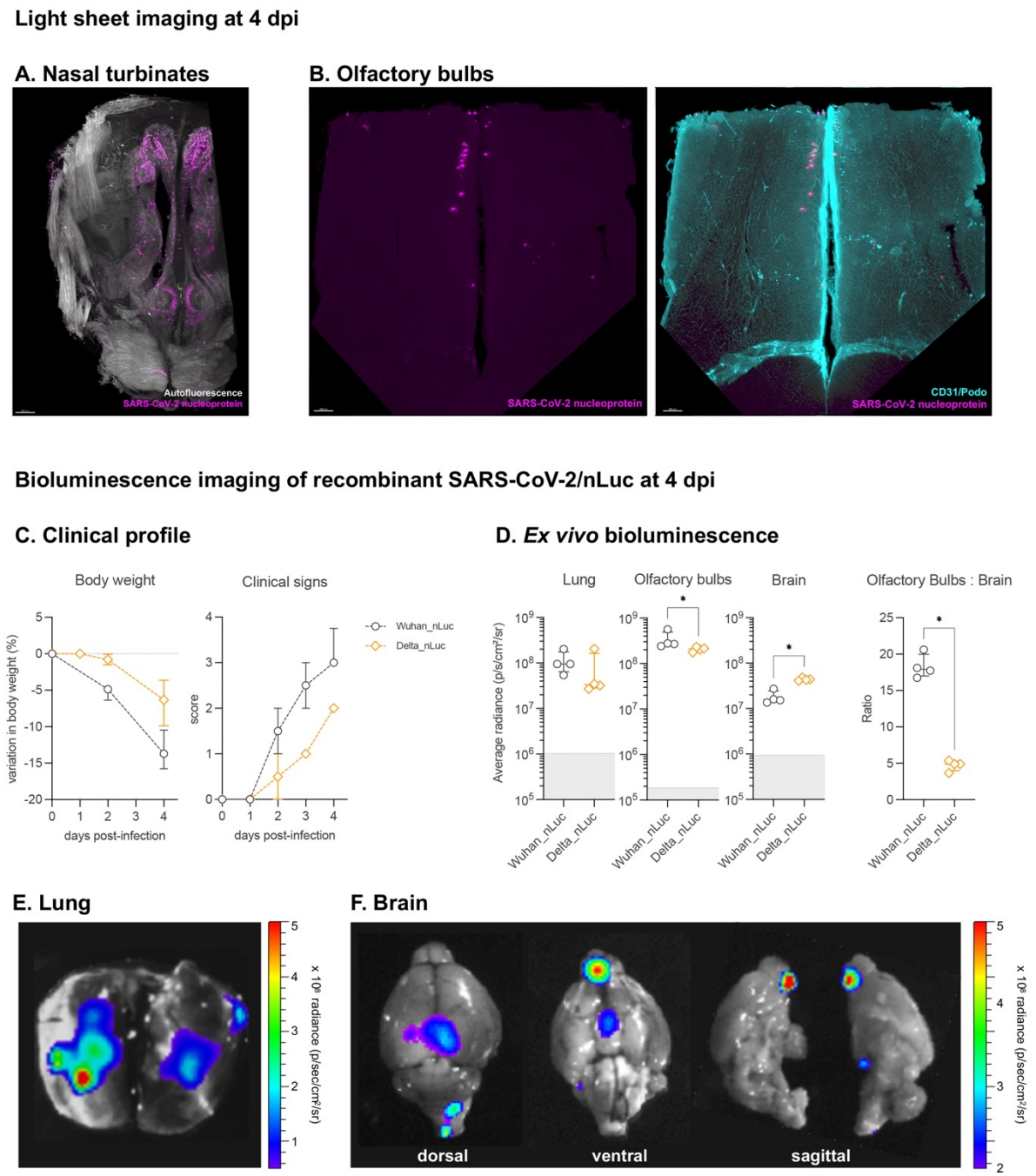

Figure 3. Imaging assessment of SARS-CoV-2 neuroinvasion. AB. iDISCO+ whole head clearing and immunolabeling against the SARS-CoV-2 nucleoprotein in hamsters infected with the SARS-CoV-2 original virus (Wuhan) at 4 days post-infection (dpi). **A.** Representative nasal turbinate (sagittal section from the skull) showing a diffuse distribution of SARS-CoV-2. Scale bar: 500 µm. See supplementary video 1. **B.** Representative olfactory bulb section stained for SARS-CoV-2 nucleoprotein and for podoplanin (CD31/Podo) to identify the vascular compartment. Note presence of SARS-CoV-2 in olfactory bulb neurons, with no macroscopic alterations in the vascular network of the olfactory bulb. Scale bar: 200 µm. See supplementary video 2. **CF.** Bioluminescent recombinant SARS-CoV-2 viruses induce a clinical disease with infection of the olfactory bulbs. **C.** Clinical profile of hamsters infected with the recombinant viruses SARS-CoV-2 Wuhan_nLuc (based on the original SARS-CoV-2 Wuhan) and Delta_nLuc (based on the Delta variant). The body weight loss and the clinical score are comparable with those induced by wild-type viruses (n=4/group). The clinical score is based on a cumulative 0–4 scale: ruffled fur; slow movements; apathy; and absence of exploration activity (See Figure 1). **D.** *Ex vivo* bioluminescence values from the lungs, the olfactory bulbs (ventral

view), the brains (ventral view) and the ratio olfactory bulbs: brain at 4 dpi (n=4/group). Horizontal lines indicate median and the interquartile range. Mann-Whitney test (*P<0.05). The gray crosshatched area corresponds to background signals obtained from the same tissues of a mock-infected hamster. **EF.** Representative *ex vivo* imaging of a lung (C) and a brain (D) of a hamster infected with a recombinant SARS-CoV-2 expressing the nLuc at 4 dpi. Note that in the brain, the major bioluminescent focus is localized in the ventral face of olfactory bulbs. See Supplementary Figure 3.

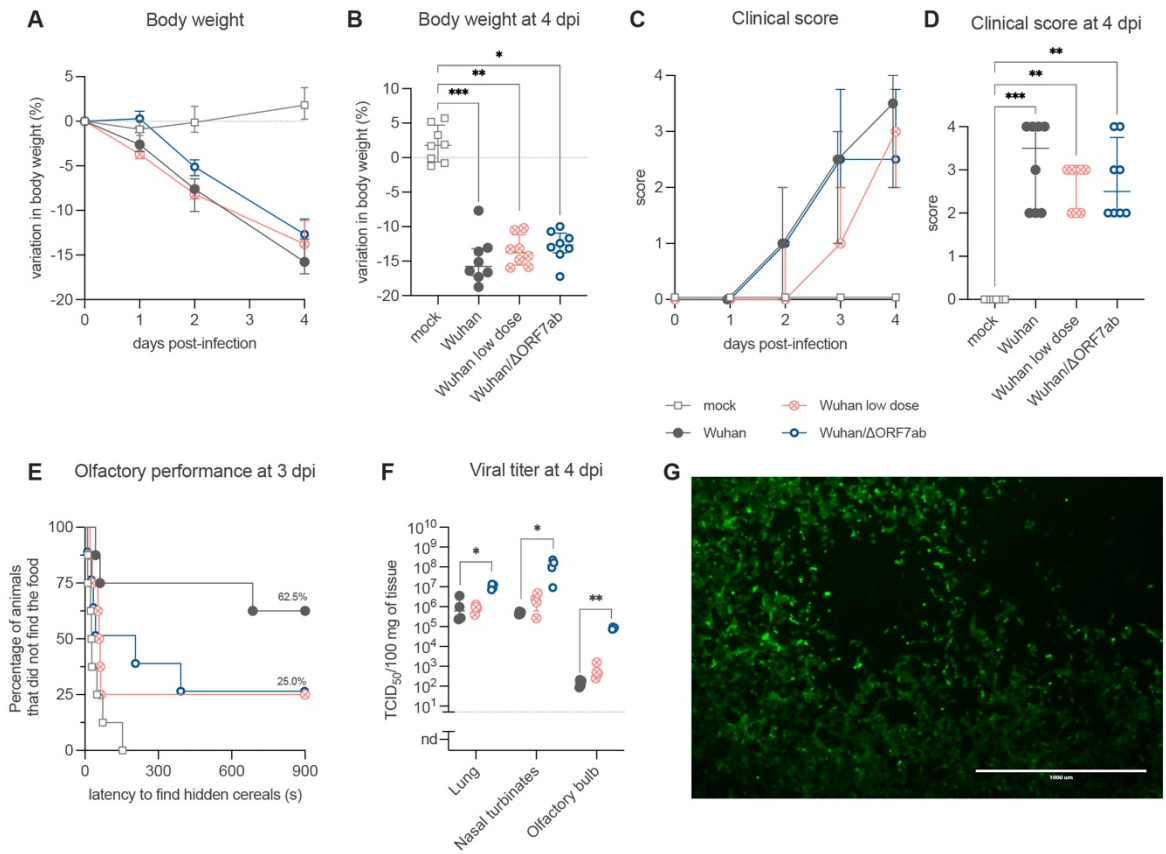

Figure 4. Clinical profile of hamsters inoculated with SARS-CoV-2 original virus (Wuhan) with a regular infectious dose (6x10^4 PFU), with a low infectious dose (6x10^2 PFU) of the SARS-CoV-2 Wuhan (Wuhan low dose), or with a regular infectious dose (6x10^4 PFU) of a SARS-CoV-2 Wuhan deleted in the ORF7ab position (Wuhan/ΔORF7ab). AB. Body weight variation over 4 days post-infection (dpi). **CD.** Clinical score comparison in the acute phase (4 dpi). The clinical score is based on a cumulative 0–4 scale: ruffled fur; slow movements; apathy; and absence of exploration activity. Horizontal lines indicate median and the interquartile range (n=8/group). **E**. Olfactory performance measured at 3 dpi. The olfaction test is based on the hidden (buried) food finding test. Curves represent the olfactory performance of animals during the test (n=8/group). **F**. Infectious viral titers in the lung, nasal turbinates and olfactory bulbs at 4 dpi expressed as $TCID_{50}$ per 100 mg of tissue. Horizontal lines indicate median and the interquartile range (n=4/group). Kruskall-Wallis test followed by the Dunn's multiple comparisons test (*P<0.05, **P<0.01, ***P<0.001). **G**. Representative image of a viral titration in the olfactory bulb from a hamster infected with Wuhan/ΔORF7ab, in which the ORF7ab has been replaced by the GFP. Note GFP+ Vero cells around a lysis plaque. Scale bar: 1000 µm. Data for SARS-CoV-2 Wuhan already presented in Figures 1 and 2.

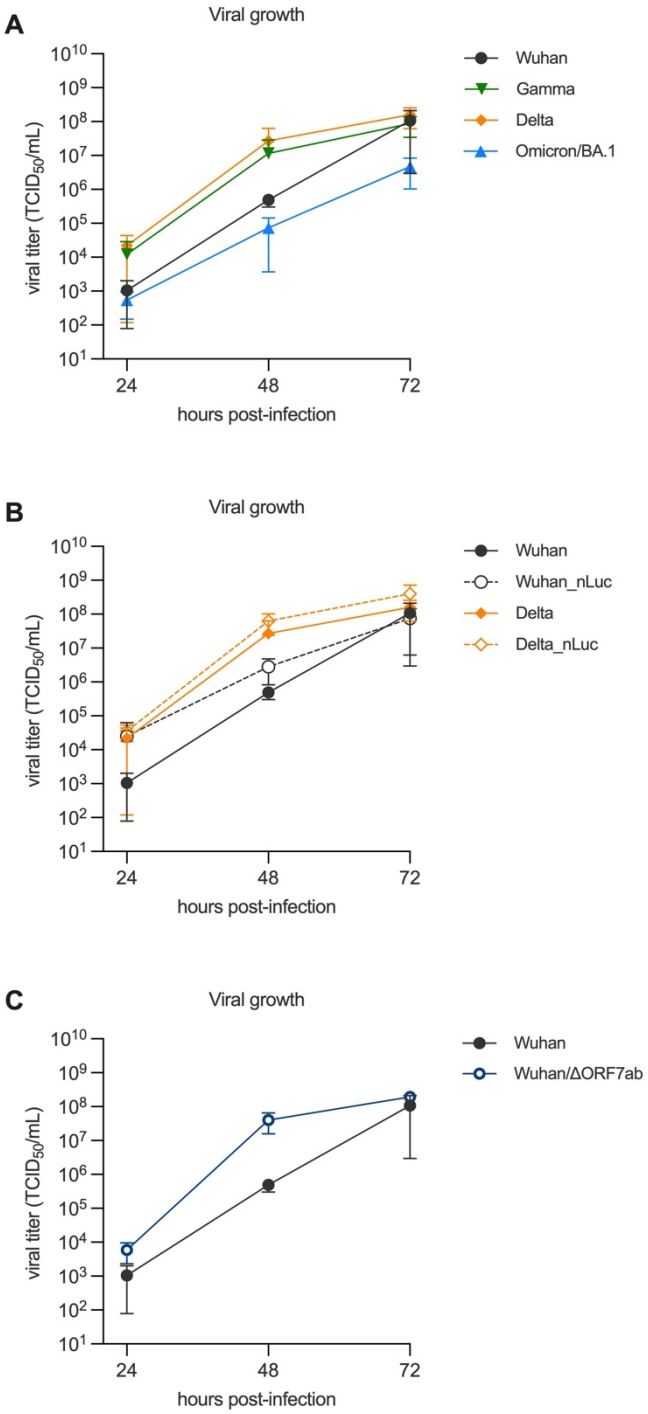

Supplementary Figure 1. *In vitro* viral growth curves of different SARS-CoV-2 viruses. A. Growth curves of the SARS-CoV-2 original virus (Wuhan) and the variants of concern (VoC) Gamma, Delta and Omicron/BA.1. **B.** Growth curves of the recombinant nanoluciferase-expressing SARS-CoV-2 viruses (Wuhan_nLuc and Delta_nLuc), in comparison with wild-type corresponding viruses. **C**. Growth curves of the SARS-CoV-2 presenting a deletion in the ORF7ab (Wuhan/ΔORF7ab), in comparison with wild-type correspondent virus. Horizontal lines indicate median and the interquartile range (n=3 independent replicates/time-point). Viral titers are expressed as the median tissue culture infectious dose ($TCID_{50}$)/mL. Related to Figures 1, 3 and 4.

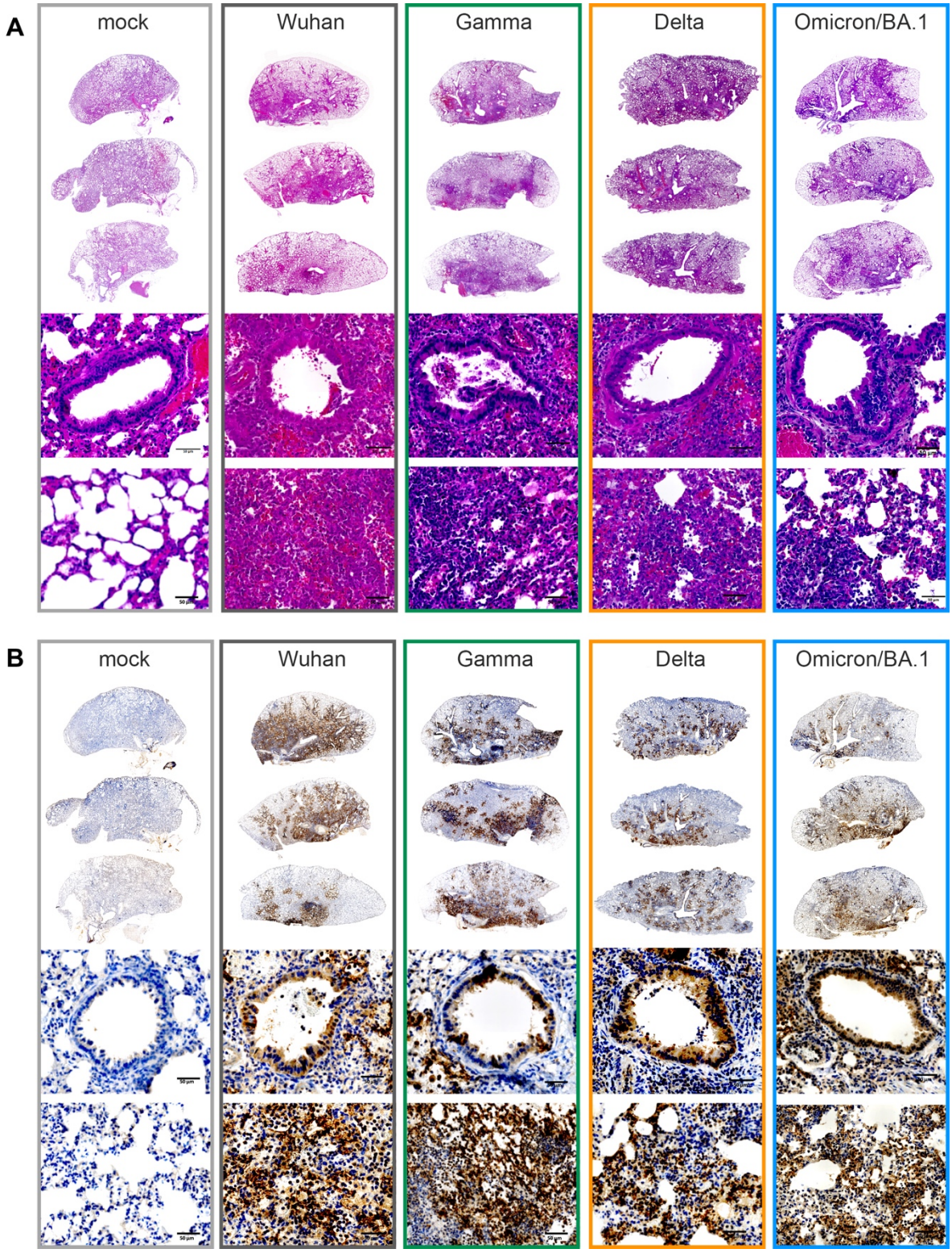

Supplementary Figure 2. Histopathology and immunohistochemical aspects of freshly-collected lungs from hamsters infected with SARS-CoV-2 original virus (Wuhan) or the variants of concern (VoC) Gamma, Delta and Omicron/BA.1 at 4 days post-infection (dpi). A. Representative images of Hematoxylin and Eosin (H&E) stained-whole lung sections (upper panels), bronchiolar epithelium (middle panels) and alveoli (bottom panels). **B.** Representative images of whole lung sections (upper panels), bronchiolar epithelium (middle panels) and alveoli (bottom panels) immuno-stained with SARS-CoV-2 N antibody. Immunoperoxidase, scale bar = 50 µm (n=8/group, except Omicron/BA.1 where n=4). Related to Figure 1.

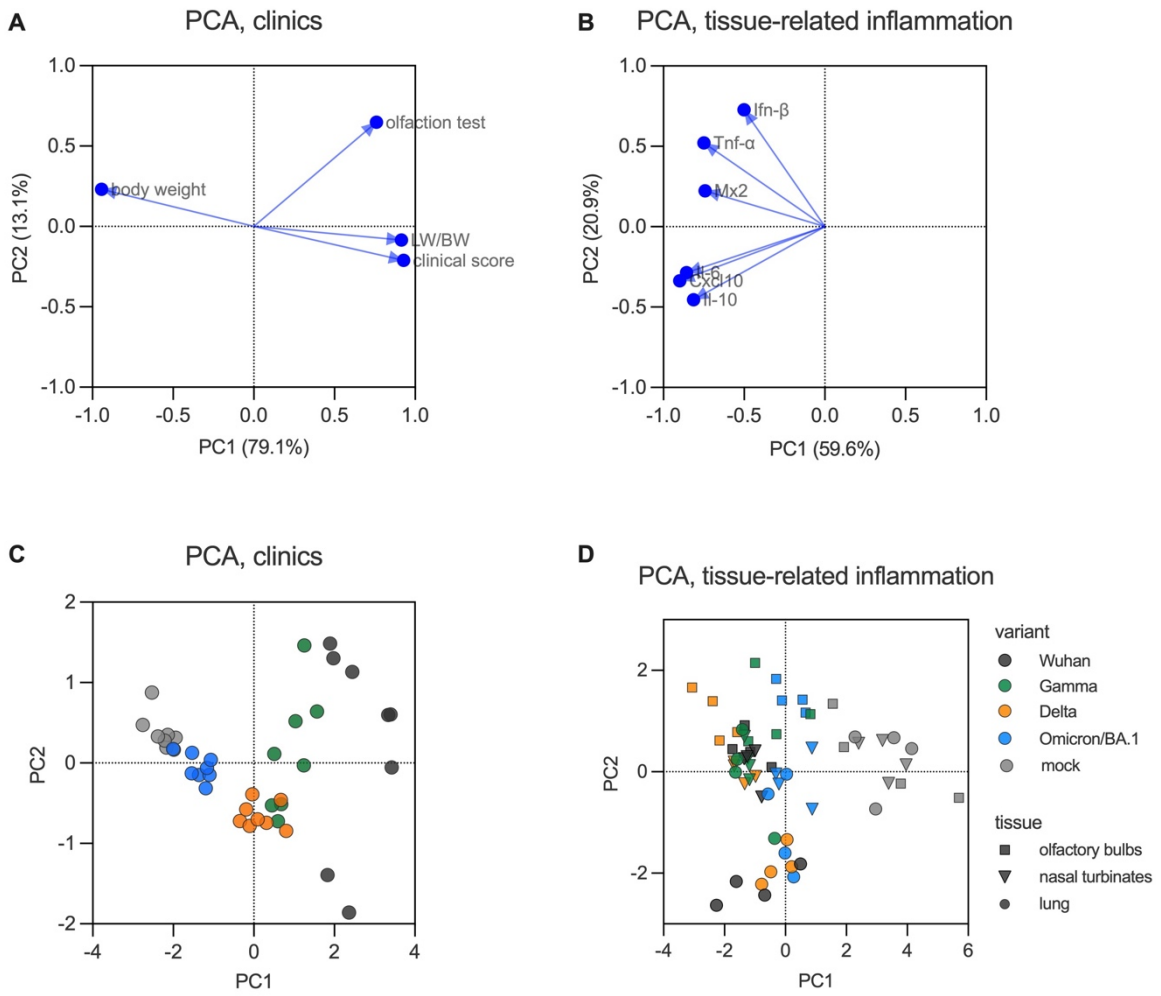

Supplementary Figure 3. Principal component analysis (PCA) of clinical parameters and immune mediators in different tissues of hamsters infected with SARS-CoV-2 original virus (Wuhan) or the variants of concern (VoC) Gamma, Delta and Omicron/BA.1. A. Variable correlation plot showing the correlation of clinical parameters in hamsters at 4 days post-infection (body weight variation, clinical score, olfaction test and lung weight-to-body weight ratio 'LW/BW'). The two-first principal components explained 92.2% of sample variability (n=8/group). **B.** Variable correlation plot showing the correlation of immune mediators' gene expression (*Mx2, Ifn-*β*, Il-6, Cxcl10, Tnf-*α and *Il-10*) in the olfactory bulb, nasal turbinates and lungs of hamsters at 4 days post-infection. The two-first principal components explained 80.5% of sample variability (n=4/group). **CD.** PCA plots. Each symbol represents one animal, colored according to the virus variant. Related to Figures 1 and 2.

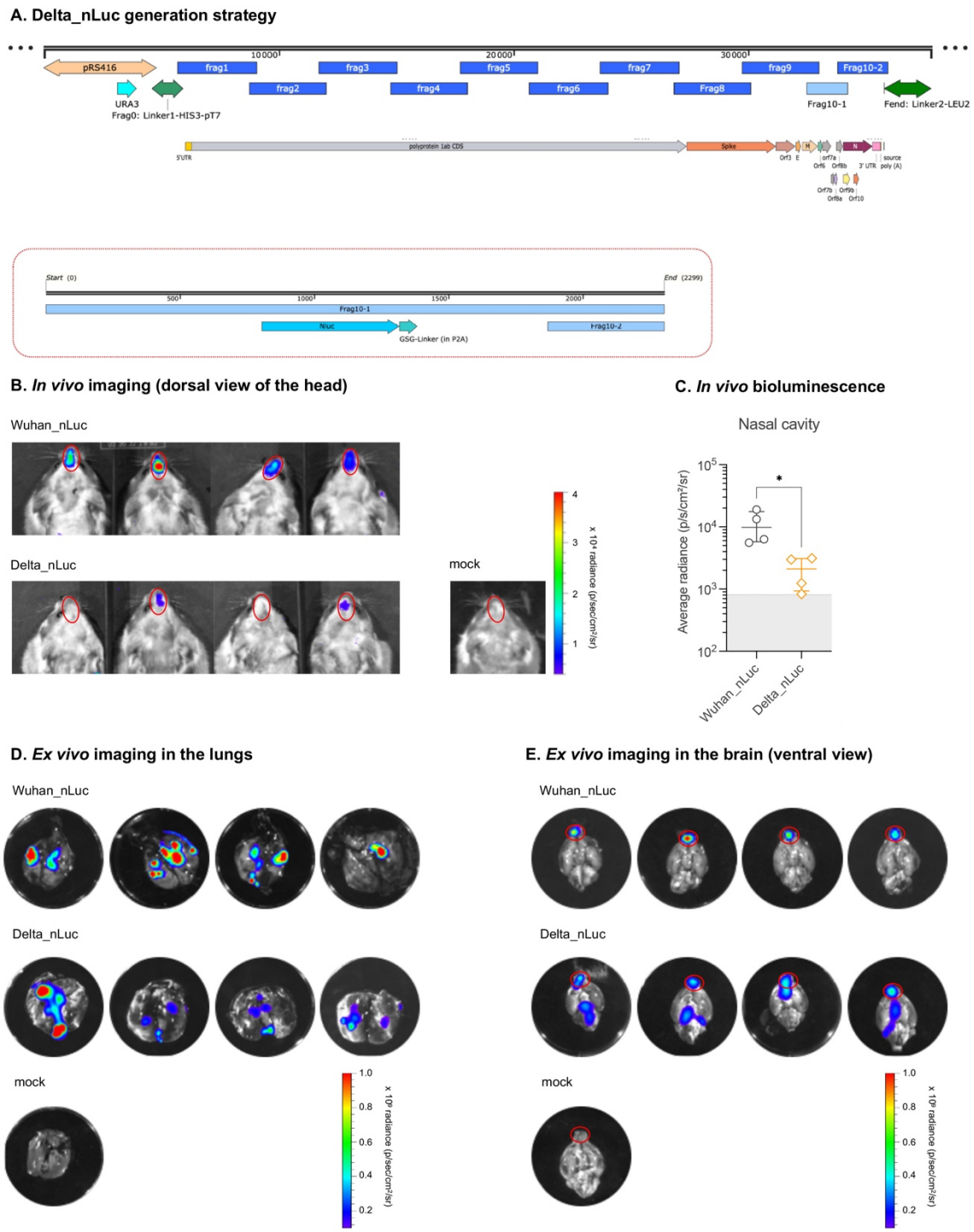

Supplementary Figure 4. *In vivo* and *ex vivo* imaging in hamsters infected with bioluminescent recombinant SARS-CoV-2 viruses at 4 days post-infection (dpi). **A.** Delta_nLuc generation strategy. **B.** *In vivo* imaging of hamsters infected with the recombinant viruses Wuhan_nLuc (based on the original SARS-CoV-2 Wuhan) and Delta_nLuc (based on the Delta). The regions of interest (ROIs) are shown as red circles (n=4/group). **C.** *In vivo* bioluminescence values from the nasal cavity (n=4/group). Horizontal lines indicate median and the interquartile range. Mann-Whitney test (*P<0.05). The gray crosshatched area corresponds to background signals obtained from a mock-infected hamster. **DE.** *Ex vivo* imaging of lungs (D) and brains (E) from hamsters infected with Wuhan_nLuc, Delta_nLuc and mock-infected at 4 dpi. The regions of interest (ROIs) are shown as red circles in the olfactory bulbs (for the lungs and the whole brain, the values from the whole organ were acquired). Related to Figure 3.

Supplementary Video 1. Light sheet imaging in the nasal turbinates. 3D distribution of the nucleoprotein in the nostrils of a SARS-CoV-2 Wuhan infected hamster using whole-head clearing. Related to Figure 3.

Supplementary Video 2. Light sheet imaging in the olfactory bulb. Presence of SARS-CoV-2 detected in the olfactory nerve and olfactory bulb neurons of a SARS-CoV-2 Wuhan infected hamster. Related to Figure 3.

Supplementary Table 1. Primers sequence used to amplify the different fragments for yeast recombination

Fragment	Sequence (5'-3') *		Position on the viral genome	Size
pRS416	Forward	CCAGTAATGTGGACATTGCC	/	4816
	Reverse	CATCAACGACCTTGTCTTCAGTA	/	
Linker His3	Forward	CCTGAAAGCACTTGAAGAATTCC	/	1448
	Reverse	GGTATGCTAAGGCACAGCACACT	78	
Frag1	Forward	GCCATTCATCCACAGTTGACA	in His 3	3213
	Reverse	CATGGTGCTGACAGTGGAGTCT	3183	
Frag2	Forward	TGAGCCATCGTGCCAATG	2885	3251
	Reverse	AGCCCGTCTGCTGGTATCAC	6135	
Frag3	Forward	GGTTGCCAAACCTTATCAGAAATG	5804	3339
	Reverse	TTCACCTGTTCCACAGCCTTG	9142	
Frag4	Forward	ACAGAGAGAAGATGACGCAGATAATG	8885	3251
	Reverse	GCCTGAATGGCCACGTACA	12135	
Frag5	Forward	TGCGGATGATATCTCAACTTTAACTG	11824	3311
	Reverse	AAAGGAAAGCAAAGTTTGTATTGTCA	15134	
Frag6	Forward	TGCGGATGATATCTCAACTTTAACTG	14782	3350
	Reverse	AAAGGAAAGCAAAGTTTGTATTGTCA	18131	
Frag7	Forward	TGCGGATGATATCTCAACTTTAACTG	17786	3371
	Reverse	AAAGGAAAGCAAAGTTTGTATTGTCA	21156	
Frag8	Forward	TGCGGATGATATCTCAACTTTAACTG	20932	3276
	Reverse	AAAGGAAAGCAAAGTTTGTATTGTCA	24207	
Frag9	Forward	TGCGGATGATATCTCAACTTTAACTG	23854	3253
	Reverse	AAAGGAAAGCAAAGTTTGTATTGTCA	28832	
Frag10-1	Forward	TGCGGATGATATCTCAACTTTAACTG	26589	1720
nLuc	Reverse	AAAGGAAAGCAAAGTTTGTATTGTCA	28332	
Frag10-2	Forward	TGCGGATGATATCTCAACTTTAACTG	27903	2132
	Reverse	AAAGGAAAGCAAAGTTTGTATTGTCA	in Leu 2	
Linker Leu2	Forward	TGCGGATGATATCTCAACTTTAACTG	/	2041
	Reverse	AAAGGAAAGCAAAGTTTGTATTGTCA	/	

*Based on the sequence of SARS-CoV-2 Delta/2021/I7.2 200 (GISAID ID: EPI_ISL_2029113) (Planas et al., 2021)

Supplementary Table 2. Primer sequences used for qPCR in the golden hamster tissues.

Gene	Sequence (5'-3')		Reference
	Forward	CCAGTAATGTGGACATTGCC	
Mx2	Reverse	CATCAACGACCTTGTCTTCAGTA	(Zivcec et al., 2011)
	Probe	FAM-TGTCCACCAGATCAGGCTTGGTCA-TAMRA	
	Forward	ACCCTAAAGGAAGTGCCAGA	
Ifn-β	Reverse	CCAGCTGCCAGTAATAGCTC	(Gowen et al., 2015)
	Probe	FAM-AGTTTGACTACAAGGATTAGCTTGAA-TAMRA	
	Forward	CCTGAAAGCACTTGAAGAATTCC	
Il-6	Reverse	GGTATGCTAAGGCACAGCACACT	(Zivcec *et al.*, 2011)
	Probe	FAM-AGAAGTCACCATGAGGTCTACTCGGCAAAA-TAMRA	
	Forward	GCCATTCATCCACAGTTGACA	
Cxcl10	Reverse	CATGGTGCTGACAGTGGAGTCT	(Zivcec *et al.*, 2011)
	Probe	FAM-CGTCCCGAGCCAGCCAACGA-TAMRA	
	Forward	TGAGCCATCGTGCCAATG	
Tnf-α	Reverse	AGCCCGTCTGCTGGTATCAC	(Espitia et al., 2010)
	Probe	FAM-CGGCATGTCTCTCAAAGACAACCAG-TAMRA	
	Forward	GGTTGCCAAACCTTATCAGAAATG	
Il-10	Reverse	TTCACCTGTTCCACAGCCTTG	(Espitia *et al.*, 2010)
	Probe	FAM-TGCAGCGCTGTCATCGATTTCTCCC-TAMRA	
	Forward	ACAGAGAGAAGATGACGCAGATAATG	
γ-actin	Reverse	GCCTGAATGGCCACGTACA	(Espitia *et al.*, 2010)
	Probe	FAM-TTG AAA CCT TCA ACA CCC CAG CC-TAMRA	
	Forward	TGCGGATGATATCTCAACTTTAACTG	
Hprt	Reverse	AAAGGAAAGCAAAGTTTGTATTGTCA	(Zivcec *et al.*, 2011)
	Probe	FAM-AAAGAATGTCTTGATTGTTGAAGGTAAAACTGACATTGG-TAMRA	

Materials and methods

Ethics. All animal experiments were performed according to the French legislation and in compliance with the European Communities Council Directives (2010/63/UE, French Law 2013–118, February 6, 2013) and according to the regulations of Institut Pasteur Animal Care Committees. The Animal Experimentation Ethics Committee (CETEA 89) of the Institut Pasteur approved this study (200023; APAFIS#25326-2020050617114340 v2) before experiments were initiated. Hamsters were housed by groups of 4 animals in isolators and manipulated in class III safety cabinets in the Pasteur Institute animal facilities accredited by the French Ministry of Agriculture for performing experiments on live rodents. All animals were handled in strict accordance with good animal practice.

SARS-CoV-2 virus and variants. The isolate BetaCoV/France/IDF00372/2020 (EVAg collection, Ref-SKU: 014V-03890) was kindly provided by Sylvie van der Werf. The human sample from which strain hCoV-19/Japan/TY7-501/2021 (Brazilian variant, JPN [P.1]) was supplied by the Japanese National Institute of Infectious Diseases (Tokyo, Japan). The isolate SARS-CoV-2 Delta/2021/I7.2 200 (Indian variant, GISAID ID: EPI_ISL_2029113) and the isolate SARS-CoV-2 Omicron/B.1.1.529 (Omicron BA.1 variant, GISAID ID: EPI_ISL_6794907) were supplied by the Virus and Immunity Unit hosted by Institut Pasteur and headed by Olivier Schwartz (Planas et al., 2022; Planas *et al.*, 2021). Viral stocks were produced on Vero-E6 cells infected at a multiplicity of infection of $1x10^{-4}$ PFU/cell. The virus was harvested 3 days post-infection, clarified and then aliquoted before storage at -80°C. Viral stocks were titrated on Vero-E6 cells by classical plaque assays using semisolid overlays (Avicel, RC581-NFDR080I, DuPont) (Baer and Kehn-Hall, 2014).
Recombinant viruses expressing Nanoluciferase (nLuc) as a reporter gene were obtained by reverse genetics. Wuhan_nLuc was derived from the clone synSARS-CoV-2-GFP-P2A-ORF7a (clone #41) generated as described (Kouprina and Larionov, 2016; Kouprina et al., 2020; Noskov et al., 2003; Noskov et al., 2011; Thi Nhu Thao et al., 2020), where the GFP reporter gene was replaced by the nLuc one. The cloning strategy was optimized to build a complete cDNA of the Delta_nLuc virus on the same backbone than the isolate EPI_ISL_2029113. SARS-CoV-2 Wuhan/ΔORF7ab was obtained using the same reverse genetic system by replacing the complete ORF7ab sequence by that of GFP.

Generation of the complete genome of SARS- CoV-2/Delta_nLuc virus. The viral genome was divided in 11 overlapping fragments around 3kb each. Those fragments and two fragments coding for different yeast-specific selection genes (His3 and Leu2) were recombined in the yeast centromere plasmid pRS416 to generate the complete genome clone of recombinant virus. The T7 promotor was

placed just before the 5'UTR sequence and a unique restriction site EAG1 was placed just after the poly(A) tail.

Viral fragments were obtained either by RT-PCR on RNA extracted from Vero-E6 cells infected by Delta using the SuperScript IV VILO Master Mix (#11756050, Thermofisher) according to the manufacturer protocol, or using synthetic genes (GeneArt, Life Technologies). All PCR amplifications were performed using Phusion™ High-Fidelity DNA Polymerase (#F530, Thermofisher). The PCR product were cloned in Topo-TA vector and their sequences controlled by sanger sequencing. The nLuc gene was inserted upstream ORF7a and separated from it using a GSG linker and a P2A peptide sequence to mediate cleavage between the reporter and the viral protein. It was directly synthetized in the F10-1 fragment.

Yeast recombination. Recombination of the 4 yeast specific fragments and the 11 viral fragments was performed on *S. cerevisiae* BY4740. A yeast culture was carried out from an overnight pre-culture in YPDA medium (2 mL of pre-culture in 50 mL of YPDA medium heated to 30° C) until the exponential growth phase was reached with an optical density corresponding to approximately $1x10^8$ cells/mL. The yeasts were harvested by centrifugation of 50 mL of culture (5,000 rpm at 4°C during 5 min) before being washed a first time in sterile solution of Tris-EDTA and lithium Acetate TE/LiAc (Tris-HCl pH 7.5 10 mM; EDTA pH 7.5 0.1 mM; LiAc 100 mM), then all the cells were resuspended in 500 µL of TE/LiAc solution (2.10^9 cells/mL). The yeast suspension was then incubated at 30° C without stirring during 30 min. During this time, a mix of all DNA fragments in an equimolar proportion was prepared. For each recombination condition, 50 µL of competent cells (10^8 cells) were brought into contact with 300 µL of TE/LiAc solution and polyethylene glycol TE/LiAc/PEG (TE 10X; LiAc 10X; PEG 3350 40% v/v) with the DNA mix to be recombined and 50 µg of salmon sperm denaturated DNA (31149, Sigma) and then cooled for at least 5 min on ice. The mixture was incubated at 30°C during 30 min without agitation before undergoing a thermal shock at 42°C during 20 min. After cooling on ice, the yeasts were pelleted by centrifugation at 2,000 rpm at RT during 5 min and then resuspended and incubated with 500 µL of 5mM CaCl2 at RT during 10 min. The yeasts were centrifuged and resuspended in 200 µL of sterile water before being plated out on a box of synthetic minimal selective medium defined by SD-His-Ura-Leu- agarose without histidine, Uracy3 and Leucine-2. The yeasts were left to grow for 3 days at 30°C. For each recombination, ten different clones were checked by multiplex PCR (#206143, Qiagen) on rapid DNA preparations carried out by the Chellex technique as already described (Thi Nhu Thao *et al.*, 2020) using specific primers (Table S1) to control the presence of the different fragments in a good orientation. The yeast colony of interest was subcultured in 200 mL of SD-His-Ura-Leu- medium to purify the plasmid.

Rescue of the virus. The plasmid was linearized by EagI-HF (#R3505, NEB) digestion, purified by a phenol chloroform process and transcribed *in vitro* into RNA using the T7 RiboMaxTM Large Scale RNA Production System (#P1300, Promega) and the m7G(5')ppp(5')G RNA Cap Structure Analog (#S1411, NEB) kits. Approximately 5 µg of linear DNA were used as template in a reaction volume of 50 µL comprising: 10 µL of 5X T7 transcription buffer; 5 µL of m7G(50)ppp(50)G RNA cap analog structure at 30 mM; 0.75 µL of 100 mM GTP; 3.75 µL of each nucleotide type ATP, CTP; 100 mM UTP; and 5 µL of RNasin T7 RNA polymerase enzyme. The reaction was incubated at 30°C during 3 h then the template DNA was digested at 37°C during 20 min by adding 2 µL of the enzyme RQ1 RNase free DNase. The synthesized RNA was finally purified using a classical phenol chloroform method and precipitated. Twelve µg of complete viral mRNA and 4 µg of plasmid encoding the viral nucleoprotein (N) gene were electroporated on $8x10^6$ Vero-E6 cells resuspended in 0.8 mL of Mirus Bio™ Ingenio™ Electroporation Solution (#MIR50114) using the Gene Pulser Xcell Electroporation System (#1652660, Biorad) with a pulse of 270V and 950 µF. The cells were then transferred to a T75 culture flask with 15 mL of DMEM supplemented with 2% FCS (v/v). The electroporated cells were incubated at 37°C, 5% CO2 for several days until the cytopathic effect (CPE) was observed. Then, the supernatant was harvested, aliquoted and frozen at -80°C until titration. The viral sequence was controlled by NGS.

Viral growth curves. Vero-E6 cells (ATCC #CRL-1586) were used to assess the replication kinetics of different SARS-CoV-2 variants and recombinant viruses. The cells were maintained in Dulbecco's modified culture medium (DMEM, 31966-021, Gibco) supplemented with 5% fetal calf serum, at 37°C in 5% CO2. On the day before infection, $1x10^6$ VeroE6 cells/well were plated onto 6-well plates. On day of infection, the cells were infected with SARS-CoV-2 virus at a multiplicity of infection (MOI) of 0.01, in independent triplicates, and incubated during 24-, 48- or 72-hours post-infection. The supernatants were collected at each time-point and frozen at -80°C. Viral titers were obtained by classical $TCID_{50}$ method on Vero-E6 cells after 72 hours post-infection (Lindenbach, 2009).

SARS-CoV-2 model in golden Syrian hamsters. Male golden Syrian hamsters (*Mesocricetus auratus;* RjHan:AURA) of 5-6 weeks of age (average weight 60-80 grams) were purchased from Janvier Laboratories and handled under specific pathogen-free conditions. The animals were housed and manipulated in isolators in a biosafety level-3 facility, with *ad libitum* access to water and food. Before any manipulation, animals underwent an acclimation period of one week. Animals were anesthetized with an intraperitoneal injection of 200 mg/kg ketamine (Imalgène 1000, Merial) and 10 mg/kg xylazine (Rompun, Bayer), and 100 µL of physiological solution containing $6x10^4$ PFU of SARS-CoV-2 (wild-type or recombinant) was administered intranasally to each animal (50 µL/nostril).

Mock-infected animals received the physiological solution only. Infected and mock-infected hamsters were housed in separate isolators and were followed-up daily during four days at which the body weight and the clinical score were noted. The clinical score was based on a cumulative 0-4 scale: ruffled fur, slow movements, apathy, absence of exploration activity. At day 3 post-infection (dpi), animals underwent a food finding test to assess olfaction as previously described (de Melo *et al.*, 2021; Lazarini et al., 2012). Briefly, 24 hours before testing, hamsters were fasted and then individually placed into a fresh cage (37 x 29 x 18 cm) with clean standard bedding for 10 minutes. Subsequently, hamsters were placed in another similar cage for 2 minutes when about 5 pieces of cereals were hidden in 1.5 cm bedding in a corner of the test cage. The tested hamsters were then placed in the opposite corner and the latency to find the food (defined as the time to locate cereals and start digging) was recorded using a chronometer. The test was carried out during a 15 min period. As soon as food was uncovered, hamsters were removed from the cage. The tests were realized in isolators in a Biosafety level-3 facility that were specially equipped for that. At 4 dpi, animals were euthanized with an excess of anesthetics (ketamine and xylazine) and exsanguination (AVMA, 2020), and samples of nasal turbinates, lungs and olfactory bulbs were collected and immediately frozen at -80°C. Fragments of lungs were also collected and fixed in 10% neutral-buffered formalin.

SARS-CoV-2 detection in golden hamsters' tissues. Frozen lung fragments, nasal turbinates and olfactory bulbs were weighted and homogenized with 1 mL of ice-cold DMEM supplemented with 1% penicillin/streptomycin (15140148, Thermo Fisher) in Lysing Matrix M 2 mL tubes (116923050-CF, MP Biomedicals) using the FastPrep-24™ system (MP Biomedicals), and the following scheme: homogenization at 4.0 m/s during 20 sec, incubation at 4°C during 2 min, and new homogenization at 4.0 m/s during 20 sec. The tubes were centrifuged at 10.000 x g during 2 min at 4°C, and the supernatants collected. Viral titers were obtained by classical $TCID_{50}$ method on Vero-E6 cells after 72 hours post-infection (Lindenbach, 2009). Viral RNA loads were obtained by the quantification of genomic and sub-genomic SARS-CoV-2 RNA based on the E gene (Corman et al., 2020). Briefly, 125 µL of the supernatants were homogenized with 375 µL of Trizol LS (10296028, Invitrogen) and total RNA was extracted using the Direct-zol RNA MicroPrep Kit (R2062, Zymo Research: nasal turbinates and olfactory bulbs) or MiniPrep Kit (R2052, Zymo Research: lung). We used the Taqman one-step qRT-PCR (Invitrogen 11732-020) in a final volume of 12.5 µL per reaction in 384-wells PCR plates using a thermocycler (QuantStudio 6 Flex, Applied Biosystems). Briefly, 2.5 µL of RNA were added to 10 µL of a master mix containing 6.25 µL of 2X reaction mix, 0.2 µL of $MgSO_4$ (50 mM), 0.5 µL of Superscript III RT/Platinum Taq Mix (2 UI/µL) and 3.05 µL of nuclease-free water containing 400 nM of primers and 200 nM of probe. To detect the genomic RNA, we used the E_sarbeco primers and probe (E_Sarbeco_F1 5'-ACAGGTACGTTAATAGTTAATAGCGT-3'; E_Sarbeco_R2 5'-

ATATTGCAGCAGTACGCACACA-3'; E_Sarbeco_Probe FAM-5'-ACACTAGCCATCCTTACTGCGCTTCG-3'-TAMRA). The detection of sub-genomic SARS-CoV-2 RNA was achieved by replacing the E_Sarbeco_F1 primer by the CoV2sgLead primer (CoV2sgLead-Fw 5'-CGATCTCTTGTAGATCTGTTCTC-3'). A synthetic gene encoding the PCR target sequences was ordered from Thermo Fisher Scientific. A PCR product was amplified using Phusion™ High-Fidelity DNA Polymerase (Thermo Fisher Scientific) and *in vitro* transcribed by means of Ribomax T7 kit (Promega). RNA was quantified using Qubit RNA HS Assay kit (Thermo Fisher scientific), normalized and used as a standard to quantify RNA absolute copy number. The amplification conditions were as follows: 55°C for 20 min, 95°C for 3 minutes, 50 cycles of 95°C for 15 s and 58°C for 30 s; followed by 40°C for 30 s.

Transcriptomics analysis in golden hamsters' tissues. RNA preparations from lungs, nasal turbinates and olfactory bulbs collected at 4 dpi were submitted to RT-qPCR. Briefly, RNA was reverse transcribed to first strand cDNA using the SuperScript™ IV VILO™ Master Mix (11766050, Invitrogen). qPCR was performed in a final volume of 10 µL per reaction in 384-well PCR plates using a thermocycler (QuantStudio 6 Flex, Applied Biosystems). Briefly, 2.5 µL of cDNA (12.5 ng) were added to 7.5 µL of a master mix containing 5 µL of Taqman (11732-020, Applied Biosystems) and 2.5 µL of nuclease-free water containing golden hamster's primer pairs (Table S2). The amplification conditions were as follows: 95°C for 10 min, 45 cycles of 95°C for 15 s and 60°C for 1 min; followed by a melt curve, from 60 °C to 95 °C. The *γ-actin* and the *Hprt* (hypoxanthine phosphoribosyl-transferase) genes were used as reference. Variations in gene expression were calculated as the n-fold change in expression in the tissues from the infected hamsters compared with the tissues of the mock-infected group using the $2^{-\Delta\Delta Ct}$ method (Pfaffl, 2001).

Sample staining and iDISCO+ clearing. For iDISCO+, three male and three female hamsters were infected with $6x10^4$ PFU of SARS-CoV-2/W and followed up as described above. At 4 dpi, animals were anesthetized with an intraperitoneal injection of ketamine (200 mg/kg; Imalgène 1000, Merial) and xylazine (10 mg/kg; Rompun, Bayer), and we performed a transcardial perfusion with DPBS containing heparin (5×10^3 U/mL) followed by 4% neutral-buffered formaldehyde. The whole heads were collected and stored in 4% neutral-buffered formaldehyde during one week before analysis. SARS-CoV-2 nucleocapsid was detected *in toto* in the snout and brain of infected hamsters using the iDISCO+ protocol previously published (Renier et al., 2016) with minimal modifications. All buffers were supplemented with 0,01% of sodium azide (Sigma-Aldrich). The snout, containing the olfactory mucosa and the olfactory nerve, and the brain were dissected and processed separately to optimize tissue manipulation.

All samples were first dehydrated in methanol (Sigma-Aldrich) using 20-40-60-80-100-100% dilutions in distilled water (1h to 2h each concentration). Complex lipid removal was achieved incubating the samples in a 2:1 mixture of dichloromethane (Sigma-Aldrich) and methanol overnight. Samples were then washed twice in methanol 100% and bleached overnight using a H_2O_2 5% solution in methanol. Then all samples were rehydrated using a methanol series (80-60-40-20%). To increase bone permeability, the snouts were decalcified by incubation in the Morse's solution (formic acid 45% and sodium citrate 20%). Finally, all the samples (brains and snouts) were washed in PBS, then PBS-T (PBS with 0,2% Triton X-100 [Sigma-Aldrich]) and incubated in permeabilization buffer (20% DMSO [Sigma-Aldrich] and 2.3% glycine [Sigma-Aldrich] in PBS-T) at 37°C overnight. Before immunostaining, samples were blocked (0,2% Gelatin [Sigma-Aldrich] in PBS-T) at 37°C for 24h. To reveal SARS-CoV-2 and vasculature, three primary antibodies were combined: Rabbit anti-SARS CoV2 nucleocapsid antibody (GTX135357, GeneTex) diluted 1:1000; Goat anti-CD31 (AF3628, R&D Systems) diluted 1:300; and Rat anti-Podocalyxin (MAB1556, R&D Systems) diluted 1:1000. After a 2-weeks incubation in primary antibody, the samples were washed (PBS supplemented with 0,2% tween-20 [Sigma-Aldrich] and 2U/mL heparin [Sigma-Aldrich]) and incubated 10 days with the following secondary antibodies: Donkey anti-Rabbit Alexa 555 (A-31572, Thermo Fisher Scientific), Donkey anti-Goat Alexa 647 (A-21447, Thermo Fisher Scientific) and Chicken anti-Rat Alexa 647 (A-21472, Thermo Fisher Scientific) all diluted at 1:500. All antibodies were diluted in blocking solution and incubated at 37°C with gentle shacking. After immunostaining, the samples were washed, dehydrated in methanol (20-40-60-80-100-100%), incubated for 3h in a 2:1 mixture of dichloromethane and methanol, washed twice (15 min each) in dichloromethane 100% and cleared by immersion in dibenzyl ether.

Light sheet imaging. Brain and snout samples were imaged using a LaVision Ultramicroscope II equipped with infinity-corrected objectives, laser lines OBIS-561nm 100mW and OBIS-639nm 70mW, and 595/40 and 680/30 filters for Alexa 555 and Alexa 647 respectively. The olfactory bulbs were imaged with a 4X 0,35NA objective, using a laser NA of 0,3 and a step size of 2µm obtaining images with 1,63x1,63x2µm/pixel resolution. The snouts were imaged with a 1,3X objective, adjusting the laser NA to 0,3 and step size of 5µm obtaining images with a 5x5x5µm/pixel resolution. All acquisitions were done with LaVision BioTec ImSpector Software. The 3D stacks obtained were analyzed using Bitplane Imaris 9.2 (Oxford instruments).

***In vivo* and *ex vivo* bioluminescence imaging.** At 4 dpi, animals infected with SARS-CoV-2/Wuhan_nLuc and SARS-CoV-2/Delta_nLuc were anesthetized with an intraperitoneal injection of ketamine (200 mg/kg; Imalgène 1000, Merial) and xylazine (10 mg/kg; Rompun, Bayer). Next, 0.45

µmoles of the nLuc substract (Nano-Glo® *in vivo* substrate, CS320501, Promega) fluorofurimazine (FFz) were injected interperitoneally and the animals were placed in a confinement box and imaged using an IVIS® Spectrum *In Vivo* Imaging System (PerkinElmer) within 5 minutes of FFz injection. Two-dimensional bioluminescence images were recorded, and photon emission was quantified (p/s/cm^2/sr) in a region of interest defined using Living Image software (PerkinElmer). After *in vivo* imaging, animals were euthanized, the lungs and the brains were collected and quickly placed in a six-wells plate. The plates were placed in a confinement box and imaged as described above.

Histopathology and Immunohistochemistry. Lung fragments fixed 7 days in 10% neutral-buffered formalin were embedded in paraffin. Four-µm-thick sections were cut and stained with hematoxylin and eosin staining. IHC were performed on Leica Bond RX using anti SARS Nucleocapsid Protein antibody (NB100-56576, Novus Biologicals) and biotinylated goat anti-rabbit Ig secondary antibody (E0432, Dako, Agilent). Slides were then scanned using Axioscan Z1 slide scanner (Zeiss) and images were analyzed with the Zen 2.6 software (Zeiss).

Statistics. Statistical analysis was performed using Prism software (GraphPad, version 9.0.0, San Diego, USA), with $p < 0.05$ considered significant. Quantitative data was compared across groups using Log-rank test, two-tailed Mann-Whitney test or Kruskall-Wallis test followed by the Dunn's multiple comparisons test. Multivariate statistical analyses on clinical parameters and on tissue inflammation were achieved using Principal Component Analysis. Randomization and blinding were not possible due to pre-defined housing conditions (separated isolators between infected and non-infected animals). *Ex vivo* analyses were blinded (coded samples).

Acknowledgements

The SARS-CoV-2 strain was supplied by the National Reference Centre for Respiratory Viruses hosted by Institut Pasteur (Paris, France) and headed by Pr. Sylvie van der Werf. The human sample from which strain 2019-nCoV/IDF0372/2020 was isolated has been provided by Dr. X. Lescure and Pr. Y. Yazdanpanah from the Bichat Hospital (Paris, France). The human sample from which strain hCoV-19/Japan/TY7-501/2021 (Gamma variant, JPN [P.1]) was supplied by the Japanese National Institute of Infectious Diseases (Tokyo, Japan). The isolate SARS-CoV-2 Delta/2021/I7.2 200 (Delta variant, GISAID ID: EPI_ISL_2029113) and the isolate SARS-CoV-2 Omicron/B.1.1.529 (Omicron BA.1 variant, GISAID ID: EPI_ISL_6794907) were supplied by the Virus and Immunity Unit hosted by Institut Pasteur and headed by Pr. Olivier Schwartz. We thank Sanjay Vashee from the J. Craig Venter Institute (Rockville, MD, USA) for the YCpBAC-his3 plasmid. This work was supported by Institut Pasteur's Task Force SARS-CoV-2 (NeuroCovid Project), by SARS-CoV-2 joint call Institut Pasteur - Paris Brain

Institute (CoVessel Project), by Institut Pasteur's Programme Fédérateur de Recherche 1 (PFR-1 - Reverse Genetics). G.D.M. acknowledges funding from the Fondation pour la Recherche Médicale (grant ANRS MIE202112015304). V.P. is recipient of a fellowship from the European Union's Horizon 2020 Framework Programme for Research and Innovation under Specific Grant Agreement No. 945539 (Human Brain Project SGA3). F.A. is recipient of a fellowship from Institut Pasteur's Programme Fédérateur de Recherche 5 (PFR-5 - Functional Genomics of the Viral Cycle). E.S.L and R.K acknowledge support from the Institut Pasteur's Task Force (project SABSOS). E.S.L acknowledges funding from the INCEPTION programme (Investissements d'Avenir grant ANR-16-CONV-0005). We would like to thank Johan Bedel for the help with histopathology. We also thank Emeline Perthame for her insights on statistical analyses. Part of this work was performed at the UtechS Photonic BioImaging (PBI) platform supported by Institut Pasteur and by Région Ile-de-France (program DIM1Health).

Author Contributions

Conceptualization: G.D.M., F.L., and H.B.

Methodology: G.D.M., R.K., V.T., N.R., and F.L.

Investigation: G.D.M., V.P., F.A., A.V.P., S.K., L.K., M.T., A.P., and A.T.

Funding Acquisition: G.D.M., M.L., P.M.L., N.R., F.L., and H.B.

Resources: B.S.T., D.H., N.W., S.M., R.K., E.S.L., N.R., V.T., and F.L.

Supervision: H.B.

Writing – Original Draft: G.D.M., and H.B.

Writing – Review & Editing: all authors

Conflict of interests

The authors declare no competing interests.

REFERENCES

Abdelnabi, R., Foo, C.S., Zhang, X., Lemmens, V., Maes, P., Slechten, B., Raymenants, J., André, E., Weynand, B., Dallmeier, K., and Neyts, J. (2022). The omicron (B.1.1.529) SARS-CoV-2 variant of concern does not readily infect Syrian hamsters. Antiviral Res *198*, 105253. https://doi.org/10.1016/j.antiviral.2022.105253.

Aliyari, S.R., Quanquin, N., Pernet, O., Zhang, S., Wang, L., and Cheng, G. (2022). The Evolutionary Dance between Innate Host Antiviral Pathways and SARS-CoV-2. Pathogens *11*, 538.

Armando, F., Beythien, G., Kaiser, F.K., Allnoch, L., Heydemann, L., Rosiak, M., Becker, S., Gonzalez-Hernandez, M., Lamers, M.M., Haagmans, B.L., et al. (2022). SARS-CoV-2 Omicron variant

causes mild pathology in the upper and lower respiratory tract of hamsters. Nature Commun *13*, 3519. 10.1038/s41467-022-31200-y.

AVMA. (2020). AVMA Guidelines for the Euthanasia of Animals: 2020 Edition* (American Veterinary Medical Association).

Baer, A., and Kehn-Hall, K. (2014). Viral Concentration Determination Through Plaque Assays: Using Traditional and Novel Overlay Systems. JoVE, e52065. doi:10.3791/52065.

Bauer, L., Laksono, B.M., de Vrij, F.M.S., Kushner, S.A., Harschnitz, O., and van Riel, D. (2022a). The neuroinvasiveness, neurotropism, and neurovirulence of SARS-CoV-2. Trends in Neurosciences *45*, 358-368. 10.1016/j.tins.2022.02.006.

Bauer, L., Rissmann, M., Benavides, F.F.W., Leijten, L., Begeman, L., Kroeze, E.V., van Run, P., Koopmans, M.P.G., Rockx, B., and van Riel, D. (2022b). Differences in neuroinflammation in the olfactory bulb between D614G, Delta and Omicron BA.1 SARS-CoV-2 variants in the hamster model. bioRxiv, 2022.2003.2024.485596. 10.1101/2022.03.24.485596.

Boscolo-Rizzo, P., Tirelli, G., Meloni, P., Hopkins, C., Madeddu, G., De Vito, A., Gardenal, N., Valentinotti, R., Tofanelli, M., Borsetto, D., et al. (2022). Coronavirus disease 2019 (COVID-19)–related smell and taste impairment with widespread diffusion of severe acute respiratory syndrome–coronavirus-2 (SARS-CoV-2) Omicron variant. International Forum of Allergy & Rhinology, 1-9. https://doi.org/10.1002/alr.22995.

Bourgon, C., Albin, A.S., Ando-Grard, O., Costa, B.D., Domain, R., Korkmaz, B., Klonjkowski, B., Poder, S.L., and Meunier, N. (2022). Neutrophils initiate the destruction of the olfactory epithelium during SARS-CoV-2 infection in hamsters. bioRxiv, 2022.2003.2015.484439. 10.1101/2022.03.15.484439.

Bryche, B., St Albin, A., Murri, S., Lacôte, S., Pulido, C., Ar Gouilh, M., Lesellier, S., Servat, A., Wasniewski, M., Picard-Meyer, E., et al. (2020). Massive transient damage of the olfactory epithelium associated with infection of sustentacular cells by SARS-CoV-2 in golden Syrian hamsters. Brain Behav Immun *89*, 579-586. 10.1016/j.bbi.2020.06.032.

Bulfamante, G., Bocci, T., Falleni, M., Campiglio, L., Coppola, S., Tosi, D., Chiumello, D., and Priori, A. (2021). Brainstem neuropathology in two cases of COVID-19: SARS-CoV-2 trafficking between brain and lung. Journal of Neurology *268*, 4486-4491. 10.1007/s00415-021-10604-8.

Cardoso, C.C., Rossi, Á.D., Galliez, R.M., Faffe, D.S., Tanuri, A., and Castiñeiras, T.M.P.P. (2022). Olfactory Dysfunction in Patients With Mild COVID-19 During Gamma, Delta, and Omicron Waves in Rio de Janeiro, Brazil. JAMA. 10.1001/jama.2022.11006.

Chan, J.F., Zhang, A.J., Yuan, S., Poon, V.K., Chan, C.C., Lee, A.C., Chan, W.M., Fan, Z., Tsoi, H.W., Wen, L., et al. (2020). Simulation of the clinical and pathological manifestations of Coronavirus

Disease 2019 (COVID-19) in golden Syrian hamster model: implications for disease pathogenesis and transmissibility. Clin Infect Dis. 10.1093/cid/ciaa325.

Chen, M., Pekosz, A., Villano, J.S., Shen, W., Zhou, R., Kulaga, H., Li, Z., Beck, S.E., Witwer, K.W., Mankowski, J.L., et al. (2022). Evolution of nasal and olfactory infection characteristics of SARS-CoV-2 variants. bioRxiv, 2022.2004.2012.487379. 10.1101/2022.04.12.487379.

Chou, S.H.-Y., Beghi, E., Helbok, R., Moro, E., Sampson, J., Altamirano, V., Mainali, S., Bassetti, C., Suarez, J.I., McNett, M., et al. (2021). Global Incidence of Neurological Manifestations Among Patients Hospitalized With COVID-19—A Report for the GCS-NeuroCOVID Consortium and the ENERGY Consortium. JAMA Network Open *4*, e2112131-e2112131. 10.1001/jamanetworkopen.2021.12131.

Christensen, P.A., Olsen, R.J., Long, S.W., Snehal, R., Davis, J.J., Ojeda Saavedra, M., Reppond, K., Shyer, M.N., Cambric, J., Gadd, R., et al. (2022). Signals of Significantly Increased Vaccine Breakthrough, Decreased Hospitalization Rates, and Less Severe Disease in Patients with Coronavirus Disease 2019 Caused by the Omicron Variant of Severe Acute Respiratory Syndrome Coronavirus 2 in Houston, Texas. The American Journal of Pathology *192*, 642-652. https://doi.org/10.1016/j.ajpath.2022.01.007.

Corman, V.M., Landt, O., Kaiser, M., Molenkamp, R., Meijer, A., Chu, D.K., Bleicker, T., Brünink, S., Schneider, J., Schmidt, M.L., et al. (2020). Detection of 2019 novel coronavirus (2019-nCoV) by real-time RT-PCR. Euro Surveill *25*, 2000045. 10.2807/1560-7917.ES.2020.25.3.2000045.

de Melo, G.D., Lazarini, F., Levallois, S., Hautefort, C., Michel, V., Larrous, F., Verillaud, B., Aparicio, C., Wagner, S., Gheusi, G., et al. (2021). COVID-19-related anosmia is associated with viral persistence and inflammation in human olfactory epithelium and brain infection in hamsters. Science Translational Medicine *13*, eabf8396.

DosSantos, M.F., Devalle, S., Aran, V., Capra, D., Roque, N.R., Coelho-Aguiar, J.d.M., Spohr, T.C.L.d.S.e., Subilhaga, J.G., Pereira, C.M., D'Andrea Meira, I., et al. (2020). Neuromechanisms of SARS-CoV-2: A Review. Frontiers in Neuroanatomy *14*. 10.3389/fnana.2020.00037.

Douaud, G., Lee, S., Alfaro-Almagro, F., Arthofer, C., Wang, C., McCarthy, P., Lange, F., Andersson, J.L.R., Griffanti, L., Duff, E., et al. (2022). SARS-CoV-2 is associated with changes in brain structure in UK Biobank. Nature *604*, 697-707. 10.1038/s41586-022-04569-5.

Dubé, M., Le Coupanec, A., Wong, A.H.M., Rini, J.M., Desforges, M., and Talbot, P.J. (2018). Axonal Transport Enables Neuron-to-Neuron Propagation of Human Coronavirus OC43. J Virol *92*. 10.1128/jvi.00404-18.

Espitia, C.M., Zhao, W., Saldarriaga, O., Osorio, Y., Harrison, L.M., Cappello, M., Travi, B.L., and Melby, P.C. (2010). Duplex real-time reverse transcriptase PCR to determine cytokine mRNA

expression in a hamster model of New World cutaneous leishmaniasis. BMC Immunology *11*, 31. 10.1186/1471-2172-11-31.

Fogeron, M.-L., Montserret, R., Zehnder, J., Nguyen, M.-H., Dujardin, M., Brigandat, L., Cole, L., Ninot-Pedrosa, M., Lecoq, L., Meier, B.H., and Böckmann, A. (2021). SARS-CoV-2 ORF7b: is a bat virus protein homologue a major cause of COVID-19 symptoms? bioRxiv, 2021.2002.2005.428650. 10.1101/2021.02.05.428650.

Frere, J.J., Serafini, R.A., Pryce, K.D., Zazhytska, M., Oishi, K., Golynker, I., Panis, M., Zimering, J., Horiuchi, S., Hoagland, D.A., et al. (2022). SARS-CoV-2 infection in hamsters and humans results in lasting and unique systemic perturbations post recovery. Science Translational Medicine *0*, eabq3059. doi:10.1126/scitranslmed.abq3059.

Garrett, N., Tapley, A., Andriesen, J., Seocharan, I., Fisher, L.H., Bunts, L., Espy, N., Wallis, C.L., Randhawa, A.K., Ketter, N., et al. (2022). High Rate of Asymptomatic Carriage Associated with Variant Strain Omicron. medRxiv, 2021.2012.2020.21268130. 10.1101/2021.12.20.21268130.

Gowen, B.B., Westover, J.B., Sefing, E.J., Bailey, K.W., Nishiyama, S., Wandersee, L., Scharton, D., Jung, K.-H., and Ikegami, T. (2015). MP-12 virus containing the clone 13 deletion in the NSs gene prevents lethal disease when administered after Rift Valley fever virus infection in hamsters. Front Microbiol *6*. 10.3389/fmicb.2015.00651.

Halfmann, P.J., Iida, S., Iwatsuki-Horimoto, K., Maemura, T., Kiso, M., Scheaffer, S.M., Darling, T.L., Joshi, A., Loeber, S., Singh, G., et al. (2022). SARS-CoV-2 Omicron virus causes attenuated disease in mice and hamsters. Nature *603*, 687-692. 10.1038/s41586-022-04441-6.

Hayn, M., Hirschenberger, M., Koepke, L., Nchioua, R., Straub, J.H., Klute, S., Hunszinger, V., Zech, F., Prelli Bozzo, C., Aftab, W., et al. (2021). Systematic functional analysis of SARS-CoV-2 proteins uncovers viral innate immune antagonists and remaining vulnerabilities. Cell reports *35*, 109126. https://doi.org/10.1016/j.celrep.2021.109126.

Helms, J., Kremer, S., Merdji, H., Clere-Jehl, R., Schenck, M., Kummerlen, C., Collange, O., Boulay, C., Fafi-Kremer, S., Ohana, M., et al. (2020). Neurologic Features in Severe SARS-CoV-2 Infection. N Engl J Med *382*, 2268-2270. 10.1056/NEJMc2008597.

Hui, K.P.Y., Ho, J.C.W., Cheung, M.-c., Ng, K.-c., Ching, R.H.H., Lai, K.-l., Kam, T.T., Gu, H., Sit, K.-Y., Hsin, M.K.Y., et al. (2022). SARS-CoV-2 Omicron variant replication in human bronchus and lung ex vivo. Nature *603*, 715-720. 10.1038/s41586-022-04479-6.

Imai, M., Iwatsuki-Horimoto, K., Hatta, M., Loeber, S., Halfmann, P.J., Nakajima, N., Watanabe, T., Ujie, M., Takahashi, K., Ito, M., et al. (2020). Syrian hamsters as a small animal model for SARS-CoV-2 infection and countermeasure development. Proc Natl Acad Sci U S A *117*, 16587-16595. 10.1073/pnas.2009799117.

Jelley, L., Douglas, J., Ren, X., Winter, D., McNeill, A., Huang, S., French, N., Welch, D., Hadfield, J., de Ligt, J., and Geoghegan, J.L. (2022). Genomic epidemiology of Delta SARS-CoV-2 during transition from elimination to suppression in Aotearoa New Zealand. Nature Commun *13*, 4035. 10.1038/s41467-022-31784-5.

Käufer, C., Schreiber, C.S., Hartke, A.-S., Denden, I., Stanelle-Bertram, S., Beck, S., Kouassi, N.M., Beythien, G., Becker, K., Schreiner, T., et al. (2022). Microgliosis and neuronal proteinopathy in brain persist beyond viral clearance in SARS-CoV-2 hamster model. eBioMedicine *79*, 103999. https://doi.org/10.1016/j.ebiom.2022.103999.

Khan, M., Yoo, S.-J., Clijsters, M., Backaert, W., Vanstapel, A., Speleman, K., Lietaer, C., Choi, S., Hether, T.D., Marcelis, L., et al. (2021). Visualizing in deceased COVID-19 patients how SARS-CoV-2 attacks the respiratory and olfactory mucosae but spares the olfactory bulb. Cell. https://doi.org/10.1016/j.cell.2021.10.027.

Kim, D.-K., Weller, B., Lin, C.-W., Sheykhkarimli, D., Knapp, J.J., Kishore, N., Sauer, M., Rayhan, A., Young, V., Marin-de la Rosa, N., et al. (2021). A map of binary SARS-CoV-2 protein interactions implicates host immune regulation and ubiquitination. bioRxiv, 2021.2003.2015.433877. 10.1101/2021.03.15.433877.

Kishimoto-Urata, M., Urata, S., Kagoya, R., Imamura, F., Nagayama, S., Reyna, R.A., Maruyama, J., Yamasoba, T., Kondo, K., Hasegawa-Ishii, S., and Paessler, S. (2022). Prolonged and extended impacts of SARS-CoV-2 on the olfactory neurocircuit. Sci Rep *12*, 5728. 10.1038/s41598-022-09731-7.

Klimek, L., Hagemann, J., Döge, J., Freudelsperger, L., Cuevas, M., Klimek, F., and Hummel, T. (2022). Olfactory and gustatory disorders in COVID-19. Allergo Journal International. 10.1007/s40629-022-00216-7.

Kouprina, N., and Larionov, V. (2016). Transformation-associated recombination (TAR) cloning for genomics studies and synthetic biology. Chromosoma *125*, 621-632. 10.1007/s00412-016-0588-3.

Kouprina, N., Noskov, V.N., and Larionov, V. (2020). Selective isolation of large segments from individual microbial genomes and environmental DNA samples using transformation-associated recombination cloning in yeast. Nature Protocols *15*, 734-749. 10.1038/s41596-019-0280-1.

Lazarini, F., Gabellec, M.-M., Torquet, N., and Lledo, P.-M. (2012). Early Activation of Microglia Triggers Long-Lasting Impairment of Adult Neurogenesis in the Olfactory Bulb. The Journal of Neuroscience *32*, 3652-3664. 10.1523/jneurosci.6394-11.2012.

Lindenbach, B.D. (2009). Measuring HCV Infectivity Produced in Cell Culture and In Vivo. In Hepatitis C: Methods and Protocols, H. Tang, ed. (Humana Press), pp. 329-336. 10.1007/978-1-59745-394-3_24.

Matschke, J., Lütgehetmann, M., Hagel, C., Sperhake, J.P., Schröder, A.S., Edler, C., Mushumba, H., Fitzek, A., Allweiss, L., Dandri, M., et al. (2020). Neuropathology of patients with COVID-19 in Germany: a post-mortem case series. Lancet Neurol *19*, 919-929. https://doi.org/10.1016/S1474-4422(20)30308-2.

Mazur-Panasiuk, N., Rabalski, L., Gromowski, T., Nowicki, G., Kowalski, M., Wydmanski, W., Szulc, P., Kosinski, M., Gackowska, K., Drweska-Matelska, N., et al. (2021). Expansion of a SARS-CoV-2 Delta variant with an 872 nt deletion encompassing ORF7a, ORF7b and ORF8, Poland, July to August 2021. Euro Surveill *26*, 2100902. 10.2807/1560-7917.ES.2021.26.39.2100902.

McMahan, K., Giffin, V., Tostanoski, L.H., Chung, B., Siamatu, M., Suthar, M.S., Halfmann, P., Kawaoka, Y., Piedra-Mora, C., Jain, N., et al. (2022). Reduced pathogenicity of the SARS-CoV-2 omicron variant in hamsters. Med *3*, 262-268.e264. https://doi.org/10.1016/j.medj.2022.03.004.

Meinhardt, J., Radke, J., Dittmayer, C., Mothes, R., Franz, J., Laue, M., Schneider, J., Brünink, S., Hassan, O., Stenzel, W., et al. (2021). Olfactory transmucosal SARS-CoV-2 invasion as port of Central Nervous System entry in COVID-19 patients. Nat Neurosci *24*, 168-175. 10.1038/s41593-020-00758-5.

Messlinger, K., Neuhuber, W., and May, A. (2022). Activation of the trigeminal system as a likely target of SARS-CoV-2 may contribute to anosmia in COVID-19. Cephalalgia *42*, 176-180. 10.1177/03331024211036665.

Mohandas, S., Yadav, P.D., Sapkal, G., Shete, A.M., Deshpande, G., Nyayanit, D.A., Patil, D., Kadam, M., Kumar, A., Mote, C., and Jain, R. (2022). Pathogenicity of SARS-CoV-2 Omicron (R346K) variant in Syrian hamsters and its cross-neutralization with different variants of concern. eBioMedicine *79*, 103997. https://doi.org/10.1016/j.ebiom.2022.103997.

Noskov, V.N., Kouprina, N., Leem, S.-H., Ouspenski, I., Barrett, J.C., and Larionov, V. (2003). A general cloning system to selectively isolate any eukaryotic or prokaryotic genomic region in yeast. BMC Genomics *4*, 16. 10.1186/1471-2164-4-16.

Noskov, V.N., Lee, N.C.O., Larionov, V., and Kouprina, N. (2011). Rapid generation of long tandem DNA repeat arrays by homologous recombination in yeast to study their function in mammalian genomes. Biological Procedures Online *13*, 8. 10.1186/1480-9222-13-8.

Panzera, Y., Ramos, N., Frabasile, S., Calleros, L., Marandino, A., Tomás, G., Techera, C., Grecco, S., Fuques, E., Goñi, N., et al. (2021). A deletion in SARS-CoV-2 ORF7 identified in COVID-19

outbreak in Uruguay. Transboundary and emerging diseases *68*, 3075-3082. 10.1111/tbed.14002.

Paterson, R.W., Brown, R.L., Benjamin, L., Nortley, R., Wiethoff, S., Bharucha, T., Jayaseelan, D.L., Kumar, G., Raftopoulos, R.E., Zambreanu, L., et al. (2020). The emerging spectrum of COVID-19 neurology: clinical, radiological and laboratory findings. Brain : a journal of neurology *143*, 3104-3120. 10.1093/brain/awaa240.

Pellegrini, L., Albecka, A., Mallery, D.L., Kellner, M.J., Paul, D., Carter, A.P., James, L.C., and Lancaster, M.A. (2020). SARS-CoV-2 Infects the Brain Choroid Plexus and Disrupts the Blood-CSF Barrier in Human Brain Organoids. Cell Stem Cell *27*, 951-961.e955. https://doi.org/10.1016/j.stem.2020.10.001.

Pfaffl, M.W. (2001). A new mathematical model for relative quantification in real-time RT-PCR. Nucleic Acids Res *29*, e45-e45. 10.1093/nar/29.9.e45.

Planas, D., Saunders, N., Maes, P., Guivel-Benhassine, F., Planchais, C., Buchrieser, J., Bolland, W.-H., Porrot, F., Staropoli, I., Lemoine, F., et al. (2022). Considerable escape of SARS-CoV-2 Omicron to antibody neutralization. Nature *602*, 671-675. 10.1038/s41586-021-04389-z.

Planas, D., Veyer, D., Baidaliuk, A., Staropoli, I., Guivel-Benhassine, F., Rajah, M.M., Planchais, C., Porrot, F., Robillard, N., Puech, J., et al. (2021). Reduced sensitivity of SARS-CoV-2 variant Delta to antibody neutralization. Nature *596*, 276-280. 10.1038/s41586-021-03777-9.

Pyke, A.T., Nair, N., van den Hurk, A.F., Burtonclay, P., Nguyen, S., Barcelon, J., Kistler, C., Schlebusch, S., McMahon, J., and Moore, F. (2021). Replication Kinetics of B.1.351 and B.1.1.7 SARS-CoV-2 Variants of Concern Including Assessment of a B.1.1.7 Mutant Carrying a Defective ORF7a Gene. Viruses *13*. 10.3390/v13061087.

Ramani, A., Müller, L., Ostermann, P.N., Gabriel, E., Abida-Islam, P., Müller-Schiffmann, A., Mariappan, A., Goureau, O., Gruell, H., Walker, A., et al. (2020). SARS-CoV-2 targets neurons of 3D human brain organoids. EMBO J *39*, e106230. 10.15252/embj.2020106230.

Renier, N., Adams, E.L., Kirst, C., Wu, Z., Azevedo, R., Kohl, J., Autry, A.E., Kadiri, L., Umadevi Venkataraju, K., Zhou, Y., et al. (2016). Mapping of Brain Activity by Automated Volume Analysis of Immediate Early Genes. Cell *165*, 1789-1802. 10.1016/j.cell.2016.05.007.

Renier, N., Wu, Z., Simon, David J., Yang, J., Ariel, P., and Tessier-Lavigne, M. (2014). iDISCO: A Simple, Rapid Method to Immunolabel Large Tissue Samples for Volume Imaging. Cell *159*, 896-910. 10.1016/j.cell.2014.10.010.

Reyna, R.A., Kishimoto-Urata, M., Urata, S., Makishima, T., Paessler, S., and Maruyama, J. (2022). Recovery of anosmia in hamsters infected with SARS-CoV-2 is correlated with repair of the olfactory epithelium. Sci Rep *12*, 628. 10.1038/s41598-021-04622-9.

Rutkai, I., Mayer, M.G., Hellmers, L.M., Ning, B., Huang, Z., Monjure, C.J., Coyne, C., Silvestri, R., Golden, N., Hensley, K., et al. (2022). Neuropathology and virus in brain of SARS-CoV-2 infected non-human primates. Nature Commun *13*, 1745. 10.1038/s41467-022-29440-z.

Ruz-Caracuel, I., Pian-Arias, H., Corral, Í., Carretero-Barrio, I., Bueno-Sacristán, D., Pérez-Mies, B., García-Cosío, M., Caniego-Casas, T., Pizarro, D., García-Narros, M.I., et al. (2022). Neuropathological findings in fatal COVID-19 and their associated neurological clinical manifestations. Pathology. https://doi.org/10.1016/j.pathol.2022.03.006.

Schaecher, S.R., Stabenow, J., Oberle, C., Schriewer, J., Buller, R.M., Sagartz, J.E., and Pekosz, A. (2008). An immunosuppressed Syrian golden hamster model for SARS-CoV infection. Virology *380*, 312-321. https://doi.org/10.1016/j.virol.2008.07.026.

Schaecher, S.R., Touchette, E., Schriewer, J., Buller, R.M., and Pekosz, A. (2007). Severe Acute Respiratory Syndrome Coronavirus Gene 7 Products Contribute to Virus-Induced Apoptosis. Journal of Virology *81*, 11054-11068. doi:10.1128/JVI.01266-07.

Shi, J., Li, Z., Zhang, J., Xu, R., Lan, Y., Guan, J., Gao, R., Wang, Z., Lu, H., Xu, B., et al. (2022). PHEV infection: A promising model of betacoronavirus-associated neurological and olfactory dysfunction. PLoS pathogens *18*, e1010667. 10.1371/journal.ppat.1010667.

Sia, S.F., Yan, L.M., Chin, A.W.H., Fung, K., Choy, K.T., Wong, A.Y.L., Kaewpreedee, P., Perera, R., Poon, L.L.M., Nicholls, J.M., et al. (2020). Pathogenesis and transmission of SARS-CoV-2 in golden hamsters. Nature *583*, 834-838. 10.1038/s41586-020-2342-5.

Silvas, J.A., Vasquez, D.M., Park, J.-G., Chiem, K., Allué-Guardia, A., Garcia-Vilanova, A., Platt, R.N., Miorin, L., Kehrer, T., Cupic, A., et al. (2021). Contribution of SARS-CoV-2 Accessory Proteins to Viral Pathogenicity in K18 Human ACE2 Transgenic Mice. Journal of Virology *95*, e00402-00421. doi:10.1128/JVI.00402-21.

Song, E., Zhang, C., Israelow, B., Lu-Culligan, A., Prado, A.V., Skriabine, S., Lu, P., Weizman, O.-E., Liu, F., Dai, Y., et al. (2021). Neuroinvasion of SARS-CoV-2 in human and mouse brainNeuroinvasion of SARS-CoV-2 in humans and mice. Journal of Experimental Medicine *218*, e20202135. 10.1084/jem.20202135.

Su, C.-M., Wang, L., and Yoo, D. (2021). Activation of NF-κB and induction of proinflammatory cytokine expressions mediated by ORF7a protein of SARS-CoV-2. Sci Rep *11*, 13464. 10.1038/s41598-021-92941-2.

Thakur, K.T., Miller, E.H., Glendinning, M.D., Al-Dalahmah, O., Banu, M.A., Boehme, A.K., Boubour, A.L., Bruce, S.S., Chong, A.M., Claassen, J., et al. (2021). COVID-19 neuropathology at Columbia University Irving Medical Center/New York Presbyterian Hospital. Brain : a journal of neurology *144*, 2696-2708. 10.1093/brain/awab148.

Thi Nhu Thao, T., Labroussaa, F., Ebert, N., V'Kovski, P., Stalder, H., Portmann, J., Kelly, J., Steiner, S., Holwerda, M., Kratzel, A., et al. (2020). Rapid reconstruction of SARS-CoV-2 using a synthetic genomics platform. Nature *582*, 561-565. 10.1038/s41586-020-2294-9.

Ueha, R., Ito, T., Furukawa, R., Kitabatake, M., Ouji-Sageshima, N., Ueha, S., Koyama, M., Uranaka, T., Kondo, K., and Yamasoba, T. (2022). Oral SARS-CoV-2 Inoculation Causes Nasal Viral Infection Leading to Olfactory Bulb Infection: An Experimental Study. Frontiers in cellular and infection microbiology *12*. 10.3389/fcimb.2022.924725.

Urata, S., Maruyama, J., Kishimoto-Urata, M., Sattler, R.A., Cook, R., Lin, N., Yamasoba, T., Makishima, T., and Paessler, S. (2021). Regeneration Profiles of Olfactory Epithelium after SARS-CoV-2 Infection in Golden Syrian Hamsters. ACS Chem Neurosci *12*, 589-595. 10.1021/acschemneuro.0c00649.

Vihta, K.-D., Pouwels, K.B., Peto, T.E., Pritchard, E., House, T., Studley, R., Rourke, E., Cook, D., Diamond, I., Crook, D., et al. (2022). Omicron-associated changes in SARS-CoV-2 symptoms in the United Kingdom. medRxiv, 2022.2001.2018.22269082. 10.1101/2022.01.18.22269082.

WHO (2022). WHO Coronavirus Disease (COVID-19) Dashboard. https://covid19.who.int/. https://covid19.who.int/.

Yang, A.C., Kern, F., Losada, P.M., Agam, M.R., Maat, C.A., Schmartz, G.P., Fehlmann, T., Stein, J.A., Schaum, N., Lee, D.P., et al. (2021). Dysregulation of brain and choroid plexus cell types in severe COVID-19. Nature *595*, 565-571. 10.1038/s41586-021-03710-0.

Yuan, S., Ye, Z.-W., Liang, R., Tang, K., Zhang, A.J., Lu, G., Ong, C.P., Poon, V.K.M., Chan, C.C.-S., Mok, B.W.-Y., et al. (2022). Pathogenicity, transmissibility, and fitness of SARS-CoV-2 Omicron in Syrian hamsters. Science *0*, eabn8939. doi:10.1126/science.abn8939.

Zazhytska, M., Kodra, A., Hoagland, D.A., Frere, J., Fullard, J.F., Shayya, H., McArthur, N.G., Moeller, R., Uhl, S., Omer, A.D., et al. (2022). Non-cell-autonomous disruption of nuclear architecture as a potential cause of COVID-19-induced anosmia. Cell *185*, 1052-1064.e1012. 10.1016/j.cell.2022.01.024.

Zivcec, M., Safronetz, D., Haddock, E., Feldmann, H., and Ebihara, H. (2011). Validation of assays to monitor immune responses in the Syrian golden hamster (Mesocricetus auratus). J Immunol Methods *368*, 24-35. 10.1016/j.jim.2011.02.004.